Textures and chemical composition of magnetite from iron oxide-copper-gold (IOCG) and Kiruna-type iron oxide-apatite (IOA) deposits and their implications for ore genesis and magnetite classification schemes

Xiao-Wen Huang,[1,2,3,†] Georges Beaudoin[2,3]

[1]State Key Laboratory of Ore Deposit Geochemistry, Institute of Geochemistry, Chinese Academy of Sciences, Guiyang 550081, China

[2]Département de géologie et de génie géologique, Université Laval, Québec, QC G1V 0A6, Canada

[3]Research Center on the Geology and Engineering of Mineral Resources (E4m), Université Laval, Québec, QC G1V 0A6, Canada

[†]Corresponding author: e-mail, huangxiaowen2008@live.cn

Abstract

Textural and compositional data of magnetite from Igarapé Bahia, Alemao, Sossego, Salobo, and Candelaria iron oxide-copper-gold (IOCG) and El Romeral Kiruna-type iron oxide-apatite (IOA) deposits show that some magnetite grains display oscillatory zoning or have been reequilibrated by oxy-exsolution, coupled dissolution and reprecipitation (CDR) reactions, and/or recrystallization. Textures formed via CDR are most widespread in the studied samples. The original oscillatory zoning was likely derived from the crystal growth during fluctuating fluid compositions rather than variation in temperature and oxygen fugacity. The oxy-exsolution of ilmenite in magnetite is attributed to increasing oxygen fugacity and decreasing temperature with alteration and mineralization, resulting in product magnetite with lower Ti and higher V contents. Recrystallization of some magnetite grains is commonly due to high-temperature annealing that retained primary compositions. Two different types of CDR processes are defined according to textures and chemical compositions of different generations of magnetite. The first generation of magnetite (Mag-1) is an inclusion-rich and trace element-rich core, which was replaced by inclusion-poor and trace element-poor rim (Mag-2). The third generation of magnetite (Mag-3), inclusion-poor but trace element-rich, occurs as veins replacing Mag-2 along fracture or grain margin. Type 1 CDR process transforming Mag-1 to Mag-2 is more extensive and is similar to those reported in skarn deposits, whereas type 2 CDR process is local, transforming Mag-2 to Mag-3. During type 1 CDR process, minor and trace elements Si, K, Ca, Mg, Al, and Mn in magnetite are excluded and Fe contents increase to

various extents, in contrast to the type 2 CDR process which is characterized by increased contents of Si, K, Ca, Mg, Al, and Mn. Type 1 CDR process is possibly induced by the changing fluid composition and/or decreasing temperature during progressive alteration and ore formation, whereas type 2 CDR process can be interpreted as post-ore replacement due to a new pulse of magmatic-hydrothermal fluids.

The identification of magnetite core (Mag-1) with igneous origin and rim (Mag-2) with magmatic-hydrothermal origin in the Sossego IOCG and El Romeral IOA deposits supports a fluid changing from magmatic to magmatic-hydrothermal during IOCG and IOA formation and indicates a genetic link between these two deposit types. Large dataset here further demonstrate that magnetite is susceptible to textural and compositional reequilibration during high-temperature magmatic and magmatic-hydrothermal processes. The reequilibrated magnetite, particularly that after CDR processes, has geochemical patterns that may be different from its precursor, complicating the application of discrimination plots for genetic and provenance interpretation. Therefore, in situ chemical analysis of magnetite combined with textural characterization is necessary to understand the origin of magnetite in IOCG and IOA deposits.

Keywords: Magnetite textures; Trace elements; Dissolution and reprecipitation; Discriminant diagrams; IOCG-IOA

Introduction

Magnetite is an important component in a variety of iron ore deposits, including iron skarns, iron oxide-copper-gold (IOCG), iron oxide-apatite (IOA), banded iron formations (BIF), and magmatic Fe-Ti oxides (Dupuis and Beaudoin, 2011). A range of minor and trace elements such as Al, Ti, Mg, Mn, Zn, Cr, V, Ni, Co, and Ga can be incorporated into the inverse spinel structure of magnetite (Buddington and Lindsley, 1964; Frost and Lindsley, 1991; Dupuis and Beaudoin, 2011; Nadoll et al., 2014). Magnetite formed from melt/fluids with various compositions or formed under different physicochemical conditions has characteristic textures and compositions (Buddington and Lindsley, 1964; Toplis and Corgne, 2002; Dupuis and Beaudoin, 2011; Dare et al., 2012; Nadoll et al., 2014; Tan et al., 2016a). Based on trace element composition of magnetite, a series of discriminant diagrams have been proposed to distinguish magnetite with different origins, e.g., magmatic vs. hydrothermal (Dare et al., 2014, 2015; Knipping et al., 2015b) or derivation from different deposit types (Loberg and Horndahl, 1983; Singoyi et al., 2006; Dupuis and Beaudoin, 2011; Nadoll et al., 2014, 2015; Knipping et al., 2015b; Makvandi et al., 2016b; Huang et al., 2019). These diagrams have been widely used in subsequent studies (Huang et al., 2013, 2014, 2015a, b, 2016, 2018; Chen et al., 2015; Chung et al., 2015; Liu et al., 2015; Zhao and Zhou, 2015; Velasco et al., 2016; Broughm et al., 2017; Pisiak et al., 2017).

Magnetite has long been considered to be resistant to mechanical breakdown and chemical alteration and thus can be used for provenance and petrogenetic studies (Grigsby, 1990; Dare et al., 2014; Nadoll et al., 2014) and mineral exploration

(Dupuis and Beaudoin, 2011; Boutroy et al., 2014; Sappin et al., 2014; Makvandi et al., 2015, 2016a, b; Pisiak et al., 2017). However, recent studies have shown that both texture and trace element composition of igneous and hydrothermal magnetite can be significantly modified via coupled dissolution-reprecipitation (CDR) processes (Hu et al., 2014, 2015; Heidarian et al., 2016; Wen et al., 2017; Yin et al., 2017; Huang et al., 2018). Infiltration of mixed basinal brines and meteoric waters that already dissolved evaporites was proposed as an important mechanism to induce CDR reaction of magnetite in skarn deposits (Hu et al., 2014, 2015; Huang et al., 2018) and Chadormalu IOA deposit (Iran) (Heidarian et al., 2016). Wen et al. (2017) proposed the crystallization of titanite results in fracturing and pressure solution of igneous magnetite to form hydrothermal varieties. Yin et al. (2017) attributed CDR reaction of skarn magnetite to an increased oxygen fugacity and co-crystallized sulfide at far-from-equilibrium or local equilibrium conditions. Therefore, the factors inducing CDR processes of magnetite from different geological environments remain controversial. Both IOCG and IOA deposits contain large volumes of distinctly low-Ti iron oxides within rocks that have undergone extensive alkali-calcic metasomatism by hydrothermal fluids (Williams et al., 2005; Corriveau et al., 2016) and may have multiple stages and/or origins of ore-forming fluids (Knipping et al., 2015a, b; Heidarian et al., 2016; Broughm et al., 2017; Rojas et al., 2018). For example, Knipping et al. (2015a, b) identified three types of magnetite that are magmatic and hydrothermal in origin and proposed a new model for the formation of IOA deposits by flotation of magmatic magnetite suspensions. Therefore, detailed

studies on textures and chemical compositions of magnetite from IOCG and IOA deposits would shed light on the factors controlling chemical processes such as CDR and formation mechanisms for these deposits.

In this study, we present combined textural and compositional data for magnetite from five IOCG and one IOA deposits. Iron oxide-copper-gold deposits include the Igarapé Bahia, Alemao, Sossego and Salobo deposits in Brazil, the Candelaria deposit in Chile, whereas IOA deposit is represented by the El Romeral deposit in Chile. The objectives of this study are to (1) characterize the textures and composition of IOCG and IOA magnetite, (2) constrain the process and possible mechanism involved in the formation of IOCG and IOA deposits, and (3) evaluate the applicability of the existing magnetite major and trace element discrimination diagrams.

Geology of the Selected Deposits and Sample Information

Nine samples are collected from five IOCG deposits and one sample is from El Romeral IOA deposit (Table 1). These deposits are mainly distributed in Carajás Mineral Province (CMP) of Brazil and Chilean iron belt. The detailed geology and geochemistry description of the selected deposits can be found in literature. Herein, we focus on the deposit information such as host rock, hydrothermal alteration, mineral assemblages, and the composition and temperature of ore-forming fluids.

Sossego

The Sossego Cu-Au deposit in CMP of Brazil is hosted by granite, granophyric

granite, gabbro, and felsic metavolcanic rocks (Monteiro et al., 2008a, b; Xavier et al., 2012). It consists of two major groups of orebodies, Sequeirinho–Pista–Baiano (SPB) and Sossego–Curral (SC), with distinct types of hydrothermal alteration. The SPB orebodies are characterized by deep-emplaced magnetite-(apatite) and albite-actinolite-rich zones, whereas the SC orebodies have predominant potassic and chlorite alteration typical of shallow crustal levels (Monteiro et al., 2008a). The deep-emplaced Neoarchean IOCG-forming events in SPB reflect coupling of ductile sinistral transpression with NNE–directed oblique shortening and Neoarchean magmatism (~2.7 Ga), whereas the shallow-emplaced Paleoproterozoic IOCG mineralization may be related to the emplacement of ~1.88 Ga A-type granites that caused regional circulation of magmatic and externally derived fluids along crustal discontinuities (Moreto et al., 2015). Two samples 080 and 084 are collected from the SC orebodies. Sample 080 is composed of magnetite, chalcopyrite, apatite, actinolite, quartz, and calcite (Fig. 1A) or consists of magnetite, chalcopyrite, ilmenite, apatite, chlorite, calcite, and talc (Fig. 1B). Ilmenite occurs as euhedral grain associated with magnetite or exsolution lamellae within magnetite (Fig. 1B). Sample 084 has a mineral assemblage of magnetite, apatite, actinolite, quartz, and chalcopyrite (Fig. 1C).

Igarapé Bahia

The Igarapé Bahia Cu-Au deposit in CMP of Brazil is hosted by Archean low-grade metamorphosed volcano-sedimentary rocks (Tazava and De Oliveira, 2000).

Hydrothermal alteration at Igarapé Bahia includes (1) Fe metasomatism leading to the formation of grunerite, fayalite, and/or Fe oxides (magnetite and/or hematite), (2) carbonate alteration (mainly siderite), (3) chalcopyrite and bornite, (4) quartz-poor gangue, (5) low REE, and (6) enrichment in U and Co from early to late (Tazava and De Oliveira, 2000; Tallarico et al., 2005; Dreher et al., 2008). This deposit was derived from magmatic-hydrothermal fluids related to Archean A-type granites (Tallarico et al., 2005). The mixing between high-temperature, high-salinity magmatic fluids and meteoric fluids is the main mechanism for the Cu-Au mineralization (Tallarico et al., 2005). One sample F392 from this deposit has a mineral assemblage of magnetite, chalcopyrite, siderite, and chlorite (Fig. 1D).

Alemao

The Alemao Cu-Au deposit in CMP of Brazil is hosted by Archean metavolcano-sedimentary rocks similar to neighboring Igarapé Bahia deposit. The orebody is conformably emplaced at the interface between volcanic rocks and the overlying sedimentary domain (Ronzê et al., 2000). Hydrothermal alteration at Alemao includes (1) Fe metasomatism leading to the formation of grunerite, fayalite, and/or Fe oxides (magnetite and/or hematite), (2) intense chloritization (Mg and Fe chlorite), (3) biotitization, (4) chalcopyrite and bornite, (5) intense carbonate alteration (mainly siderite), and (6) local silicification and tourmalinization from early to late (Ronzê et al., 2000). This deposit was considered to be related to magmatic-hydrothermal system similar to that responsible for IOCG deposits in CMP

(Ronzê et al., 2000). One sample Alemao from this deposit has a mineral assemblage of magnetite, apatite, quartz, calcite ± chlorite (Fig. 1E, F). Some magnetite grains show obvious core-rim textures composed of inclusion-rich core and inclusion-poor rim (Fig. 1E). Chalcopyrite inclusions are common in magnetite.

Salobo

The Salobo Cu-Au-Ag deposit in CMP of Brazil is hosted by the Archean volcano-sedimentary rocks consisting of amphibolite, metagraywacke, banded iron formation, and quartzite (Requia and Fontboté, 2000). The ore-bearing, magnetite-rich rocks are the product of strong Fe–K alteration at high temperatures (550–650°C) and have been deformed and mylonitized (Lindenmayer and Teixeira, 1999; Requia and Fontboté, 2000; Requia et al., 2003). The Fe–K alteration is replaced by widespread chlorite alteration (<370°C) accompanied by the formation of calcite, epidote, albite, sericite, quartz, and fluorite (Xavier et al., 2012). The main Cu-Au ores were probably formed by high temperature, highly saline, oxidized, sulfur-poor, near-neutral pH fluids (Requia, 2002), related to Archean (~2.57 Ga) granite magmatism (Requia et al., 2003). The main Cu-Au mineralization was overprint by ~2.45 Ga hydrothermal activity, indicating a protracted tectono-thermal event for the evolution of the Salobo deposit (deMelo et al., 2017). Total homogenization temperatures of highly saline fluid inclusions in quartz range from 173°C to 485°C and geothermometry from post-ore stage chlorite yields a temperature of 350°C (Réquia and Xavier, 1995). Sample SAL2 from this deposit is

composed of magnetite, chalcopyrite, grunerite, and quartz (Fig. 1G), whereas sample 11CC051 consists of magnetite, chalcopyrite, chlorite, and quartz (Fig. 1H).

Candelaria

The Candelaria Cu-Au-Ag deposit in the southeast of Copiapó, Chile is the largest IOCG deposit in the Punta del Cobre belt (Marschik and Fontboté, 2001). This deposit is hosted by Early Cretaceous volcanic and volcaniclastic rocks. Alkali metasomatism is widespread in Candelaria, including sodic (albite and/or marialitic scapolite) or K–Fe (biotite and/or K-feldspar) alteration related to ore formation (Marschik and Fontboté, 2001; Marschik et al., 2003). The Cu–Fe (chalcopyrite + magnetite ± hematite) ores are associated with biotite–potassium feldspar ± calcic amphibole ± epidote alteration at Candelaria (Marschik and Fontboté, 2001). Magnetite tends to be associated with potassic assemblages and hematite is common in sodium metasomatized rocks, which are interpreted in terms of more internal and high-temperature vs. external and low-temperature portions of the ore-forming hydrothermal system (Marschik and Fontboté, 2001). The bulk of the magnetite probably formed at temperatures of about 500°C to 600°C, whereas the main sulfide stage followed with formation of pyrite and chalcopyrite at temperatures of >470°C to 328°C (Marschik and Fontboté, 2001). Magmatic fluids or non-magmatic fluids equilibrated with magmatic silicates were dominant during the main copper mineralization, which are mixed with a non-magmatic fluid (e.g., basinal brines or meteoric waters) during the late stages of hydrothermal activity (Marschik and

Fontboté, 2001). Ore formation was broadly coeval with batholithic granitoid intrusions and with regional uplift, suggesting a magmatic fluid contribution into the hydrothermal system (Marschik and Fontboté, 2001). Sample 367A from this deposit consists of magnetite, K-feldspar, actinolite, and minor albite and biotite (Fig. 1I). Sample PC98102 is composed of magnetite, chalcopyrite, and minor chlorite, biotite, and monazite (Fig. 1J). Sample PC1492 has a mineral assemblage of magnetite, chalcopyrite, K-feldspar, actinolite, chlorite, and apatite (Fig. 1K).

El Romeral

The ~110 Ma El Romeral deposit (Rojas et al., 2018) is one of several IOA deposits (e.g. Cerro Negro Norte, Los Algarrobos, Los Colorados) that form the Chilean iron belt. The deposit is hosted by Late Palaeozoic metasediments cut by Early Cretaceous andesite porphyry and diorite (Bookstrom, 1977). The hydrothermal alteration in this deposit is represented by actinolitization, hloritization, argillization, and martitization (Bookstrom, 1977). Magnetite deposition was accompanied by pervasive actinolitization, followed by chloritization and alteration of previously actinolitized diorite and phyllite. Altered rocks within and around the orebodies contain magnetite, actinolite, plagioclase, diopside, clinozoisite, titanite, chlorapatite, marialitic scapolite, tourmaline, chlorite, pyrite, calcite, mica, and clays (Bookstrom, 1977). The deposit was considered to be produced by magmatic-hydrothermal fluids derived from the Romeral diorite (Bookstrom, 1977; Rojas et al., 2018) or basin-derived, non-magmatic brines (Mathur et al., 2002). One sample El Romeral from this deposit

consists of magnetite, actinolite, and minor chlorite and biotite (Fig. 1L).

Analytical Method

All samples were prepared as standard polished thin sections and subsequently examined using optical microscopy and back-scattered electron (BSE) imaging to characterize the mineralogical and textural relationships. BSE was done using a HITACHI S-3400N scanning electron microscope (SEM) attached with an Oxford Instruments Energy+ energy dispersive spectrometer (EDS) hosted at the Université du Québec à Montréal (UQAM). Major and minor/trace element analyses of magnetite were conducted at Université Laval using a CAMECA SX-100 electron probe microanalyzer (EPMA), equipped with five wavelength-dispersive spectrometers. Major element Fe was determined using a 5-µm diameter beam with a voltage of 15 kV and a current of 20 nA. A series of minor and trace elements were measured, including K, Ca, Al, Si, Ti, Mg, Mn, Cr, V, Sn, Cu, Zn, Ni, and P, using 5-µm diameter beam with a voltage of 15 kV and a current of 100 nA. Analytical conditions are similar to those described by Dupuis and Beaudoin (2011). Calibration was achieved using a range of natural and synthetic standards, comprising simple oxides (GEO Standard Block of P and H Developments) and natural minerals (Mineral Standard Mount MINM 25–53, Astimex Scientific) (Jarosewich et al., 1980). The background was measured on one side of the peak for 15-20 s at a position free of interfering element X-ray and the concentration was counted over the peak for 20-40 s depending on the element. Detection limits are ~450 ppm for Fe, ~100 ppm for Zn,

~80 ppm for Cu, ~60 ppm for Ni, 40-50 ppm for V, Cr, Mn, Sn, and 15-25 ppm for K, Ca, Ti, Al, Si, Mg, and P. Wavelength dispersive spectrometer (WDS) X-ray maps were collected using a beam diameter of 1 μm, an accelerating voltage of 15 kV, a beam current of 100 nA, and a counting time of 20 ms/pixel with a resolution of 512 × 512 pixels.

Magnetite Petrography

Four main textures have been recognized in the studied magnetite samples, including oxy-exsolution, oscillatory zoning, coupled dissolution-reprecipitation, and recrystallization textures (Table 1). Exsolution lamellae (trellis type or needle-like) of ilmenite were observed in sample 080 from the Sossego IOCG deposit (Fig. 2A, B). Magnetite grains in sample 080 formed during three generations. The primary magnetite (Mag-1) in the core, with ilmenite exsolution, is commonly overgrown by low-Ti magnetite at the rim (Mag-2) (Fig. 2A). The third generation of magnetite (Mag-3), with darker gray in BSE images (lower mean Z number), partly replaced low-Ti magnetite (Mag-2) and locally contains amphibole and/or rutile inclusions (Fig. 2A). But some magnetite grains in sample 080 lack of overgrowth Mag-2 and show core with ilmenite lamellae (Mag-1) replaced by Mag-3 along grain margin (Fig. 2B). Sample 084 contains two generations of magnetite. The first generation of magnetite in sample 084 is composed of dark gray (Mag-1D) and light gray (Mag-1L) zones that image oscillatory zoning (Fig. 2C, D). Ilmenite and hercynite occur as inclusions in the first generation of magnetite (Fig. 2C, D). The zoned magnetite was locally

replaced by the second generation of magnetite (Mag-2) to form irregular veins (Fig. 2C). Sample F392 from the Igarapé Bahia IOCG deposit contains two generations of magnetite (Fig. 2E). The first generation of magnetite (Mag-1) is darker under BSE and rich in siderite and chalcopyrite inclusions, whereas the second generation of magnetite (Mag-2) is smooth and inclusion-poor (Fig. 2E). Magnetite from the Alemao IOCG deposit shows typical replacement/dissolution-reprecipitation textures. Magnetite grains in this sample comprise a dark gray, inclusion-rich domain, in the core (Mag-1) surrounded by a rim of light gray, inclusion-poor domain (Mag-2) (Fig. 2F). The main inclusions in Mag-1 are quartz, chlorite, and chalcopyrite (Fig. 2F). But some dark magnetite domains lack porosity or inclusions. Both generations of magnetite are crosscut by calcite veins (Fig. 2F).

Samples 367A and PC1492 from the Candelaria IOCG deposit display dissolution-reprecipitation textures (Fig. 3A, B). Sample 367A contains two generations of magnetite. The primary magnetite (Mag-1) is dark gray and contains amounts of quartz inclusions, whereas secondary magnetite (Mag-2) is light gray and inclusion-poor (Fig. 3A). Magnetite from sample 367A shows triple junction textures that are typical of recrystallization (e.g., Hu et al., 2015) (Fig. 3A). Magnetite grains from sample PC1492 are composed of dark gray, inclusion-rich domains (Fig. 3B) replaced along grain edges by light gray, inclusion-poor domains (Fig. 3B). Magnetite grains in sample SAL2 from the Salobo IOCG deposit contain dark gray (Mag-1) and light gray (Mag-2) domains (Fig. 3C). Some quartz inclusions occur along the boundary between two generations of magnetite. Sample El Romeral from the El

Romeral IOA deposit contains three generations of magnetite. The first magnetite (Mag-1), commonly in the core, contains rutile, quartz, and chlorite inclusions and is replaced by smooth, inclusion-poor magnetite domains (Mag-2) at the rim (Fig. 3D). Mag-2 is replaced by the third generation of magnetite (Mag-3) along grain boundaries (Fig. 3D). Mag-3 is darker than Mag-1 and Mag-2 in BSE images. Sample 11CC051 from the Salobo IOCG deposit and sample PC98102 from the Candelaria IOCG deposit show triple junction recrystallization textures in magnetite (e.g., Hu et al., 2015) (Fig. 3E, F). These samples contain two generations of magnetite, inclusion-rich (Mag-1) and inclusion-poor (Mag-2) (Fig. 3E, F).

Chemical Composition of Magnetite

Major and trace element X-ray maps

We use WDS X-ray elemental maps to characterize chemical zoning of different generations of magnetite (Figs. 4-7). Sample 080 from the Sossego IOCG deposit contains three generations of magnetite that show Ti, Al, Si, Ca and Mn zoning (Fig. 4A, B). Mag-1 shows higher Ti, Al and Mn contents than Mag-2 and Mag-3, whereas Mag-3 has higher Si, Ca, and Mg contents than other two generations of magnetite. No iron zoning is observed for three generations of magnetite at 512 × 512 pixels resolution. Sample 084 from the Sossego IOCG deposit contains two generations of magnetite and the first generation of magnetite can be divided into dark and light gray zones (Mag-1D and Mag-1L) due to different Al, Si, Ca, and Mg contents (Fig. 5A, B). Titanium contents in Mag-1D and Mag-1L are heterogeneously distributed but no

Ti zoning is observed (Fig. 5A, B). The first generation of magnetite contains ilmenite and hercynite inclusions as shown by Ti and Al element maps. The second generation of magnetite (Mag-2) crosscutting Mag-1D and Mag-1L has lower Ti, Al, Si, Ca, and Mg contents (Fig. 5A). Mag-1 in sample F392 from the Igarapé Bahia IOCG deposit shows lower Fe but higher Si and Mg contents than Mag-2 (Fig. 6A). Similarly, Mag-1 from samples Alemao, 367A, and PC1492 has lower Fe but higher Si and Mg contents than Mag-2 (Fig. 6B-D). Titanium, Al, and Ca contents are indistinguishable on the X-ray maps between two generations of magnetite in these samples. Mag-3 in El Romeral sample has higher Al, Si and Ca contents than Mag-1 and Mag-2 (Fig. 7A). Moreover, Al, Si, and Ca contents in Mag-3 increase from grain margin to interior. Iron, Ti and Mg contents are indistinguishable between three generations of magnetite. Mag-1 in samples 11CC051 and PC98102 from Salobo and Candelaria IOCG deposits, respectively, have slightly higher Si, Mg, and Mn contents than Mag-2 (Fig. 7B, C).

Major and trace element compositions

Full EPMA results for magnetite are presented in Table A1. Figures 8 and 9 show comparative box and whisker diagrams of minor and trace elements in various magnetite generations, whereas Fig. 10 shows the variations of Fe contents in different generations of magnetite. In general, minor and trace elements in magnetite have contents varying from below detection limits to ~2 wt% (Figs. 8, 9). For a specific element, the contents vary up to three orders of magnitudes. Mag-1 in sample

080 from the Sossego deposit has Mn, Ti, V, and Cr contents of 0.01-0.07 wt%, 0.09-1.89 wt%, 0.17-0.21 wt%, and 0.01-0.02 wt%, respectively, higher than those of Mag-2 and Mag-3 (Table A1; Fig. 8A). Mag-3 in sample 080 shows higher Si, K, Ca, Al, and Mg contents (0.11-0.70 wt%, <0.01-0.07 wt%, 0.03-0.36 wt%, <0.01-0.36 wt%, and <0.01-1.89 wt%, respectively) than Mag-1 and Mag-2 (Fig. 8A). Mag-1D in sample 084 from the Sossego deposit has Si, K, Ca, Mn, Mg, and Ti contents of 0.17-0.65 wt%, <0.01-0.05 wt%, 0.01-0.16 wt%, 0.02-0.08 wt%, 0.07-0.18 wt%, and 0.50-1.88 wt%, respectively, higher than those of Mag-1L and Mag-2 (Fig. 8B). In general, Mag-1 in samples F392, Alemao, 367A, and PC1492 has higher Si, K, Ca, Al, Mn, and Mg contents than their respective Mag-2 (Fig. 8C-F). Due to limited data for magnetite in sample SAL2 from the Salobo deposit, the statistical result of trace element composition for two generations of magnetite is unclear (Fig. 9A). However, there is a trend where Mag-1 has higher Ca, P, and V contents than Mag-2 (Fig. 9A). Mag-3 in the El Romeral sample has higher Si, Ca, Al, Mg, and Ti contents (0.35-0.81 wt%, 0.11-0.29 wt%, 0.29-0.65 wt%, 0.03-0.08 wt%, and 0.05-0.19 wt%, respectively) than Mag-1 and Mag-2 (Fig. 9B). Mag-1 and Mag-2 in samples 11CC051 or PC98102 from the Salobo and Candelaria deposits, respectively, have similar Al, Mn, Mg, Ti, Zn, and Ni contents (Fig. 9C, D), but Mag-1 in sample PC98102 has higher Si, K, and Ca contents than Mag-2 (Fig. 9D).

Magnetite grains from all samples have Fe contents ranging from 65.8 to 71.4 wt% (Fig. 10), lower than the stoichiometric value of 72.4 wt%. Different generations of magnetite also show distinct Fe contents. Mag-3 in sample 080 has higher iron

contents (average 70.3 wt%) than Mag-1 and Mag-2 (average 69.5 wt%) (Fig. 10). Mag-1L in sample 084 has higher Fe contents (average 69.0 wt%) than Mag-1D (average 68.4 wt%), but both of them have Fe contents lower than Mag-2 (average 70.4 wt%) (Fig. 10). Mag-2 in samples F392, Alemao, 367A, PC1492, and PC98102 has higher Fe contents than Mag-1 (Fig. 10). Iron contents decrease from Mag-2, Mag-1, to Mag-3 in the El Romeral sample. Mag-1 and Mag-2 in sample SAL2 from the Salobo deposit have similar Fe contents of 70.0-70.2 wt%, whereas two generations of magnetite in sample 11CC051 from the same deposit also have similar Fe contents of 70.3-71.1 wt% (Fig. 10).

Discussion

The formation of oscillatory zoning

Oscillatory zoning in magnetite from the studied IOCG and IOA deposits is uncommon and was only observed in sample 084 from the Sossego deposit. The oscillatory zoning is composed of dark gray, Si-rich (Mag-1D) and light gray, Si-poor zones (Mag-1L) under BSE imaging (Figs. 2C, D, 11A). Similar oscillatory zoning is also observed in magnetite from Fe skarn deposits (Shimazaki, 1998; Ciobanu and Cook, 2004; Dare et al., 2014; Huang et al., 2018), the lava flows of EI Laco in Chile (Dare et al., 2015), the phreatomagmatic pipe in in the Tunguska Basin of East Siberia (Neumann et al., 2017), and the Los Colorados iron oxide-apatite deposit of Chile (Knipping et al., 2015b; Deditius et al., 2018). Ciobanu and Cook (2004) interpreted oscillatory zoning in magnetite from the Ocna de Fier-Dognecea Fe-Cu-Pb-Zn skarn

deposit in Romania as an example of autocatalytic surface attachment in a Liesegang environment, perhaps similar to experiments with minerals in solid solution series where end members have different solubility (Putnis et al., 1992). Chemical waves, as well as other types of oscillation, may develop spontaneously, especially close to thermodynamic equilibrium (Ortoleva et al., 1987; Chu and Ross, 1990; Hjelmfelt and Ross, 1991; Neumann et al., 2017). But the oscillations in chemical composition are seemingly incompatible with slow, near-equilibrium growth. Such compositional shifts appear to violate the second law of thermodynamics because systems cannot spontaneously reverse their growth composition to lower-entropy states at stable growth conditions (Shore and Fowler, 1996). This situation has given rise to various physical models that rely upon cyclic changes in pressure, temperature, or bulk composition to vary the composition of the growing crystal. Therefore, a more common explanation for the oscillatory zoning in magnetite is that growth zoning formed as a result of changes in fluid compositions and/or physicochemical parameters, such as temperature and oxygen fugacity, during crystal growth, which periodically affects the partitioning behavior of trace elements into magnetite and co-forming minerals (Shimazaki, 1998; Dare et al., 2015; Knipping et al., 2015b; Sievwright et al., 2017; Huang et al., 2018).

Oscillatory mineral zonation is usually associated with crystal growth in an open system, either a hydrothermal system or a melt, after a period of magma mixing or degassing (Holten et al., 2000). Shore and Fowler (1996) proposed extrinsic (e.g., change in solution composition, pressure, or temperature) and intrinsic (e.g.,

adsorption of growth inhibitors) mechanisms to explain the oscillatory zoning in natural magmatic and hydrothermal minerals. Similarly, Holten et al. (2000) explained zonation patterns as the result of coupling between the generally nonlinear crystal growth dynamics and the boundary conditions imposed by externally controlled fluctuations. Adsorption of growth inhibitors may play an important role, particularly at the microscopic scale in carbonate and sphalerite that formed under lower temperature conditions (Shore and Fowler, 1996). However, magnetite at the Sossego deposit formed at a relatively high temperature (~300-500°C; Monteiro et al., 2008b), preventing the adsorbed species from acting as inhibitors of the crystal growth. For different zones of oscillatory zoning in magnetite from the sample 084, dark gray domains (Mag-1D) have higher Si, K, Ca, Mn, Mg, and Ti contents but lower Fe contents than light gray domains (Mag-1L) (Figs. 5B, 8B, 10). The sharp compositional boundaries between the alternate trace element-rich and -poor zones within single magnetite grain imply preservation of the original oscillatory zoning (Figs. 2C, D, 11A), which requires the growth rate of the crystal to be higher than intracrystalline diffusion (Watson and Liang, 1995). X-ray map shows that Ti does not change synchronously with Al, Si, Ca and Mg (Fig. 5A, B), indicating that Ti chemical behavior is different from other elements during magnetite growth. The contrasting behavior of Ti was also observed in oscillatory zoning of magnetite from Los Colorados deposit (Deditius et al., 2018) and may be related to: (1) compatibility of Ti with magnetite structure; (2) the changes in the diffusivity of Ti^{4+} in the near-surface environment during magnetite growth comparing with the other elements;

and (3) mobility and/or different sources of Ti (Deditius et al., 2018). No obvious differences in Ti contents between Mag-1D and Mag-1L in X-ray map (Fig. 5A, B) indicate relatively stable temperature for their formation. But point analyses indicate Mag-1D has higher Ti contents than Mag-1L (Fig. 8). The higher Ti contents in Mag-1D may be due to the unavoidable contamination by ilmenite inclusions (Figs. 2C, D, 5A, B) or Fe-Ti oxide nanoinclusions (Deditius et al., 2018). The similar V contents in Mag-1D and Mag-1L of oscillatory zoning (Fig. 8B) imply relatively stable oxygen fugacity. Therefore, oscillatory zoning in magnetite from sample 084 was likely derived from the crystal growth during fluctuating hydrothermal fluid compositions rather than variation in temperature and oxygen fugacity (Fig. 10B).

Reequilibration textures in magnetite

Oxy-exsolution Oxy-exsolution of ilmenite is very common in magnetite from igneous rocks (Frost and Lindsley, 1991; Lindsley, 1991), metamorphic rocks (Harlov, 1992; Harlov and Hansen, 2005), and magmatic Fe-Ti-(V) and Ni-Cu-sulfide deposits (Von Gruenewaldt et al., 1985; Dare et al., 2012; Liu et al., 2015; Tan et al., 2016b). In contrast, in magmatic-hydrothermal environment, oxy-exsolution is absent and low-Ti magnetite is expected to be dominant in the IOCG, IOA, porphyry, and skarn deposits (Meinert et al., 2005; Williams et al., 2005; Groves et al., 2010; Dupuis and Beaudoin, 2011; Chen et al., 2015; Nadoll et al., 2015; Huang et al., 2016, 2017, 2018). Sample 080 from the Sossego deposit show oxy-exsolution lamellae of ilmenite in primary magnetite (Mag-1) (Fig. 2A, B), similar to exsolution textures of

igneous magnetite. Primary magnetite (Mag-1) in this samples has Ti contents up to 1.89 wt% (Table A1). The oxy-exsolution textures are also observed in the Forsyth (Canada), Iron Crown (Canada), Marmoration (Canada), Chengchao (China), and Daye (China) skarn deposits (Hu et al., 2015). Magnetite from these deposits contains up to ~1 wt% Ti (Hu et al., 2015). Since oxy-exsolution processes involve a solid state diffusion mechanism that is more favorable at a higher temperature when fluids are absent (Frost and Lindsley, 1991; Putnis, 1992, 2009), the oxy-exsolution textures observed in these high-temperature magmatic-hydrothermal deposits indicate a primary magmatic formation of some magnetite grains, as observed by Knipping et al. (2015 a, b) at Los Colorados.

In addition to temperature, oxygen fugacity (fO_2) also significantly affects the solubility of Ti in magnetite (Frost, 1991; Lindsley, 1991; Sievwright et al., 2017). For instance, at fO_2 < FMQ + 3 (FMQ, fayalite-magnetite-quartz), the partition coefficient of Ti between titanomagnetite–melt decreases with increasing fO_2 (Sievwright et al., 2017). Therefore, the high-Ti magnetite in the Sossego deposit may have originally formed at high temperatures under relatively reducing conditions, subsequently being modified through the exsolution of Fe-Ti oxides in response to increasing fO_2 and decreasing temperature during the progressive alteration and mineralization (Fig. 11B). This is consistent with the evolving temperatures and fluid compositions in the Sossego–Curral orebodies of the Sossego deposit. Monteiro et al. (2008a) showed that the Sossego–Curral orebodies experienced early K-alteration (460 ± 25 ºC), followed by infilling of veins and breccias (400 ± 50 ºC), Cu

mineralization (275 ± 25 ºC), and post-mineralization veins (250 ± 25 ºC). During these processes, fluids evolved from high-temperature formational/metamorphic or magmatic origin to low-temperature hydrothermal origin (Monteiro et al., 2008a). Oxy-exsolution of ilmenite in high-Ti magnetite results in decreased Ti and increased V contents in product magnetite (Fig. 12A).

Interface coupled dissolution-reprecipitation Dissolution-reprecipitation is a reaction, in the presence of a fluid, replacing an original phase with either an entirely new phase, or the same phase with a different composition, to reduce the free energy of a system (Putnis, 2002, 2009, 2015; Harlov et al., 2005, 2011; Ruiz-Agudo et al., 2014). When dissolution of the parent phase and precipitation of the product phase are coupled in both space and time, pseudomorphic (isovolumetric) replacement occurs in interface coupled dissolution reprecipitation (CDR) reaction (Putnis, 2009; Xia et al., 2009; Putnis and John, 2010; Ruiz-Agudo et al., 2014; Altree-Williams et al., 2015). CDR textures in magnetite have been observed in natural samples (Ciobanu and Cook, 2004; Hu et al., 2015; Makvandi et al., 2015; Heidarian et al., 2016; Broughm et al., 2017; Wen et al., 2017; Yin et al., 2017; Huang et al., 2018) and different mechanisms have been proposed to explain these textures. Experimental studies also have demonstrated that magnetite can be dissolved by chloride-rich hydrothermal fluids (Chou and Eugster, 1977; Whitney et al., 1985; Ilton and Eugster, 1989) and a significant amount of iron can also be transported by low-density aqueous vapor in the magmatic-hydrothermal environment (Simon et al., 2004). There are some key

identifying features of CDR, as outlined by Putnis (2009), including: (1) a close spatial relationship between the parent and product phases; (2) a sharp reaction front between parent and product without a diffusional profile; (3) a permeable porosity generated within the product phase; (4) transfer of crystallographic structure from the parent to the product when an epitaxial relationship exists. Different generations of magnetite in samples F392, Alemao, 367A, PC1492, SAL2, and El Romeral, form distinct domains in one magnetite grain or occur as different grains that are spatially close (Figs. 2E-F, 3A-D). Moreover, sharp boundaries are observed between different generations of magnetite. For example, the second generation of magnetite (Mag-2) in sample 084 (Fig. 2C) shows lighter BSE contrast than Mag-1D and Mag-1L and crosscuts the zoned magnetite. Magnetite has features consistent with criteria (1) and (2) of CDR textures. But whether crystallographic structures between parent and product magnetite are same needs further transmission electron microscopy study.

Porosity development in the product phase is a common feature of CDR, necessary for the propagation of dissolution within the mineral (Putnis, 2015). But product magnetite from samples F392, Alemao, PC1492, SAL2, and El Romeral lacks interconnected microscope-scale porosity (Figs. 2E-F, 3B-D). These features of magnetite from IOCG and IOA deposits are different from that of magnetite from altered granitic rocks and skarn deposits that experienced CDR processes (Hu et al., 2014, 2015; Wen et al., 2017; Yin et al., 2017). There are a number of factors that can explain lack of porosity in the product phase during CDR (Putnis and Austrheim, 2013): (1) porosity is a non-equilibrium and transient microstructure and would be

expected to anneal with time due to evolving fluid composition (Putnis et al., 2005; Putnis, 2009; Pollok et al., 2011); (2) porosity may be restricted to the parent-product interface; (3) pore scale is smaller than the SEM resolution (~10 nm) (Niedermeier et al., 2009). Although we cannot determine which factor controls the absence of observable porosity in the product magnetite, the local geological conditions would affect the textual and compositional equilibrium between parent and product phases. The destruction of textural features associated with CDR processes, such as porosity and sharp replacement fronts, can disguise evidence of pervasive fluid infiltration events (Putnis and Austrheim, 2013). This textural evolution is driven both by internal minimization of excess energy by coarsening and by external processes in which continued interaction between an infiltrating fluid and the secondary mineral phases (Hellmann et al., 2012). Compositional and textural re-equilibration in the presence of a fluid phase is usually fast in terms of geological timescales, which further contributes to masking textural evidence for extensive fluid-mediated mineral alteration (Altree-Williams et al., 2015).

It is worth noting that amounts of inclusions are found in the parent magnetite in samples 080, F392, Alemao, PC1492, and El Romeral (Figs. 2E-F, 3A-B). Ciobanu and Cook (2004) also reported a single magnetite crystal with a Si-rich, inclusion-rich core surrounded by a Si-rich, inclusion-free rim in skarn ores from Ocna de Fier-Dognecea (Romania). These textures were also observed in IOA magnetite from Missouri (Nold et al., 2014) and the Chilean Iron Belt (Knipping et al., 2015a, b; Rojas et al., 2018). They assigned the porous cores as igneous phenocrysts overgrown

by pristine magmatic-hydrothermal magnetite. The ilmenite + rutile-rich core in sample 080 and rutile-rich core in El Romeral magnetite can be interpreted as igneous core because the regular distribution of ilmenite and rutile in magnetite implies an exsolution process at a low cooling rate probably related to a magmatic event (Rojas et al., 2018). However, the inclusions in magnetite core of samples F392, Alemao, and PC1492 are mainly quartz, chlorite, albite, biotite, titanite and chalcopyrite (Figs. 2E-F, 3B), which are mainly hydrothermal in origin. EPMA analyses show that magnetite cores (Mag-1) have higher Si, Al, and Mg contents than massive domains at the rim (Mag-2) (Fig. 8C, D, F). The relatively homogenous distribution of Si, Al, and Mg in magnetite cores (Fig. 6A, B, D) indicates that these elements occur as lattice-substituted elements or nanoincluisons in magnetite (Deditius et al., 2018). Therefore, the silicate inclusion and trace element-rich cores in these magnetite grains have precipitated from Si-Al-Mg-rich hydrothermal fluids. It is suggested that the trace element-rich magnetite is more susceptible to fluid-assisted alteration because incorporation of small ionic radius cations such as Si^{4+} in magnetite would cause lattice defect or deformation (Hu et al., 2014). Development of smooth, inclusion-poor rims, in close proximity to inclusion-rich cores, thus strongly suggests that these formed from re-precipitation of the dissolved magnetite cores.

Two types of CDR processes Most of the studied samples contain two generations of magnetite, whereas samples 080 and El Romeral contain three generations of magnetite. According to the textures, composition of different generations of

magnetite, and formation conditions, we consider that there are two different CDR processes responsible for the formation of the second and third generations of magnetite (Fig. 11). First, magnetite grains experienced different CDR processes have different textures. Type 1 CDR process is the replacement process that involves the dissolution of Si-rich, primary magnetite (Mag-1) in the core and precipitation of Si-poor, secondary magnetite (Mag-2) in the rim to form core-rim texture (Figs. 2E-F, 3A-C). Type 1 CDR process is responsible for the formation of Mag-2 in samples 084，Alemao, F392, PC1492, SAL2, and 367A (Fig. 11A, C-F). Type 2 CDR process is the replacement process that the inclusion-poor, Si-rich magnetite (Mag-3) replaced inclusion-poor, Si-poor magnetite (Mag-2) along fracture or grain margins (Figs. 2A-B, 3D). Type 2 CDR process transforming Mag-2 (sometimes Mag-1 when Mag-2 is absent, Fig. 2B) to Mag-3 is local and is responsible for the formation of Mag-3 in samples 080 and El Romeral (Figs. 11B, F). Second, magnetite formed by different CDR processes has different chemical compositions. During type 1 CDR process, most of minor and trace elements such as Si, Ca, K, Al, Mn, Mg, and to a less extent Ti are excluded from the primary magnetite (Mag-1), forming the secondary variety (Mag-2) with improved iron grade (Fig. 12B). Type 1 CDR process is thus considered to be an important mechanism for increasing the iron grade in hydrothermal magnetite from skarn deposits (Hu et al., 2014, 2015; Yin et al., 2017; Huang et al., 2018), IOA deposits (Heidarian et al., 2016), and altered granitic rocks (Wen et al., 2017). In contrast to the type 1 CDR process, Mag-3 formed via the type 2 CDR process has higher Si, K, Ca, Al, Mn, and Mg contents than Mag-1 and Mag-2 (Fig. 12C).

Moreover, Mag-3 has higher Ti contents than Mag-2 (Figs. 8A, 9B).

In addition to different textures and compositions of magnetite, different factors control these two types of CDR processes. Different parameters can affect the CDR reactions, including the fluid composition, mineral solubility, temperature and pressure, Eh and pH, and oxygen and sulfur fugacities (Putnis, 2002; Putnis and Putnis, 2007; Xia et al., 2009; Putnis and John, 2010; Pollok et al., 2011; Makvandi et al., 2015). Infiltration of mixed basinal brines and meteoric waters that already dissolved evaporites was proposed as an important mechanism to induce CDR reaction of magnetite (Hu et al., 2014, 2015; Heidarian et al., 2016; Huang et al., 2018), because these externally derived fluids contributed to an increase in salinity and Cl^- contents of the ore-forming fluids, enhancing Fe solubility and consequently leading to disequilibrium between the precipitated magnetite and the evolving fluids (Chou and Eugster, 1977; Whitney et al., 1985; Ilton and Eugster, 1989). During type 1 CDR process, Ti contents in magnetite slightly decrease or keep stable whereas V contents are constant (Fig. 8C-F), indicating that changes in temperature and oxygen fugacity may be not the main factor. Alternatively, variations in fluid composition may play an important role. Considering that type 1 CDR process is commonly involved in massive magnetite associated with chalcopyrite (Fig. 1E-F) that represents main ore formation, we consider that type 1 CDR process is induced by the changing or evolving fluid composition during progressive alteration and mineralization. This conclusion is supported by the fluid composition and evolution of individual IOCG and IOA deposits. For the Sossego IOCG deposit, dilution and cooling of the hot

metalliferous fluid (>500°C) by mixing with meteoric fluids have been proposed as the main mechanisms responsible for the deposition of metals transported as metal chloride complexes (Monteiro et al., 2008b). For the Igarapé Bahia and Alemao deposits, the mixing between high-temperature, high-salinity magmatic fluids and meteoric fluids was considered to be the main mechanism for the Cu-Au mineralization (Ronzê et al., 2000; Tallarico et al., 2005). For the Candelaria deposit, dominant magmatic fluids or non-magmatic fluids equilibrated with magmatic silicates for the main copper mineralization were also mixed with a non-magmatic fluid (e.g., basinal brines or meteoric waters) during the late hydrothermal stages (Marschik and Fontboté, 2001). For type 2 CDR process, Ti, Si, K, Ca, Al, Mg, and Mn contents obviously increase (Figs. 8A, 9B, 12C), in contrast with the compositional variations during type 1 CDR process. The type 2 CDR process cannot be induced by evolving ore-forming fluids with lower temperature because contents of compatible elements such as Ti, Mg, and Mn increase (magnetite-silicate melt partition coefficients are 7.0, 2.6, and 3.0, respectively; Dare et al., 2012). Alternatively, increased temperature and/or addition of trace element-rich fluids induced this process. Type 2 CDR process commonly occurs as vein replacement along magnetite fracture or grain margin, it thus can be interpreted as local post-ore replacement due to pulse of late magmatic-hydrothermal fluids.

Recrystallization Solid-state recrystallization is a process wherein new mineral grains grow from pre-existing mineral grains by solid-state diffusion of ions in

response to change in temperature, pressure, or composition of the rock system (Urai et al., 1986; Hoskin and Black, 2000). This process commonly involves changing of the crystal fabric or crystal size without an accompanying change in mineral chemistry (Hoskin and Black, 2000). Some magnetite grains from samples 11CC051 and PC98102 show well-defined 120° triple junction (Fig. 3E, F), characteristic of mosaic texture. Mosaic textures are equilibrium textures that reflect the recrystallization of magnetite and annealing (Ciobanu and Cook, 2004; Nold et al., 2013). For example, mosaic textures in Chahgaz iron ore deposit (Bafq district, Iran) and Gol-Gohar deposit (southern Sanandaj-Sirjan belt, Iran) were interpreted to result from magmatic annealing (Foerster and Jafarzadeh, 1994; Mücke and Younessi, 1994). However, similar magnetite fabrics in iron deposits within the Bafq district were considered to be metasomatic replacement in origin (Daliran et al., 2010; Heidarian et al., 2016). High-temperature (~550ºC) annealing and recrystallization of deformed and fractured magnetite was also used to explain the mosaic texture of magnetite in massive ores of skarn deposits (Ciobanu and Cook, 2004). However, Hu et al. (2015) considered that the mosaic texture in skarn magnetite was most likely the result of fluid-assisted recrystallization process. Magnetite in samples 11CC051 and PC98102 is composed of inclusion-rich core (Mag-1) and inclusion-poor rim (Mag-2) and lacks replacement textures that occur in other magnetite samples experienced CDR processes. Weakly compositional zoning in these samples is composed of Si- and Mg-rich core and rim depleted in these elements (Fig. 7B, C). The higher Si, Mg, and K contents in the magnetite core than rim (Fig. 9C, D) may result from

contamination of micrometer mineral inclusions in terms of heterogeneous distribution of these elements (Fig. 7B, C). But Si-Mg-K-rich cores also reflect fluids responsible for core formation are relatively rich in these elements because these elements can also occur as solid solution or nano-particles in magnetite (Xu et al., 2014; Deditius et al., 2018). No obvious differences in Ca, Al, Mn, Ti, Zn, V, Ni, Cr, and Fe contents are observed between Mag-1 and Mag-2 (Figs. 9C, D, 10), resulting in indistinguishable compositional fields in the plot of Fe versus total Si+K+Ca+Al+Mn+Mg contents (Fig. 12D). Therefore, we infer that the mosaic texture of magnetite from IOCG and IOA deposits results from simultaneous recrystallization and annealing of inclusion-rich magnetite (Fig. 11F).

Implication for the formation of IOCG and IOA deposits

IOCG deposits are considered to form in upper crustal environments from volatile-rich magmatic-hydrothermal fluids exsolved from high-temperature calc-alkaline melts variably contaminated by Fe-P-Si-rich crustal rocks and evolving to A-type granites (Hitzman et al., 1992; Pollard, 2000; Sillitoe, 2003; Corriveau et al., 2007; Groves et al., 2010; Tornos, 2011). But IOCG deposits lack clear spatial associations with igneous intrusions as, for instance, displayed by porphyry and skarn deposits (Williams et al., 2005). Non-magmatic fluids, particularly an evaporitic source, are also proposed as an important fluid source for IOCG deposits (Barton and Johnson, 1996, 2000). There are several examples supporting a mixed source of magmatic fluids, basinal brines, and/or meteoric water responsible for the formation

of IOCG deposits (Haynes et al., 1995; Kendrick et al., 2007; Baker et al., 2008; Kendrick et al., 2008; Zhao and Zhou, 2011; Chen, 2013; Huang et al., 2015b; Zhao et al., 2015). There are four main genetic models for the formation of IOA deposits: (1) crystallization from high-temperature, volatile-rich oxide melts, produced by magma immiscibility and segregated from a silicate liquid (Nyström and Henríquez, 1994; Frietsch and Perdahl, 1995; Henríquez and Nyström, 1998; Naslund et al., 2002; Henríquez et al., 2003; Tornos et al., 2016; Velasco et al., 2016); (2) replacement of the host rocks by iron-rich hydrothermal fluids (Hitzman et al., 1992; Rhodes et al., 1999; Hitzman, 2000; Sillitoe and Burrows, 2002; Edfelt et al., 2005; Valley et al., 2010; Dare et al., 2015; Broughm et al., 2017). The third model is evaporitic-source model that invokes thermal circulation of highly saline fluids originating from coeval or older sources (Barton and Johnson, 1996, 2004). Magmatism provides the necessary heat and igneous rocks also serve as the source and hosts for mineralization. Evaporitic sources provide the chloride for metal transport and the Na for hydrothermal alteration, and they drive fluids toward oxidized, relatively S-poor compositions. The fourth model for IOA deposits is a combination of the first two models that igneous magnetite crystallized from intermediate silicate melt overprinted by hydrothermal magnetite derived from magmatic-hydrothermal fluids (Knipping et al., 2015a, b; Simon et al., 2018).

Oxy-exsolution of ilmenite in magnetite from Cu-Au ores is rarely reported in IOCG and IOA deposits that are characterized by low-Ti magnetite and/or hematite (Williams et al., 2005). High-Ti magnetite with oxy-exsolution textures (Mag-1) in

sample 080 from the Sossego IOCG deposit is magmatic in origin, whereas high-Ti magnetite with oscillatory zoning in sample 084 (Mag-1D and Mag-1L) is hydrothermal in origin, in spite of their similar Ti+V and Ca+Al+Mn contents (Fig. 13A). The magmatic affinity of Mag-1 in sample 080 is confirmed by the granular ilmenite in equilibrium with ilmenite (Fig. 1B) and well-developed ilmenite exsolution lamellae within magnetite (Fig. 2A, B), typical of Ti-rich magnetite or titanomagnetite in magmatic Fe-Ti oxide deposits and accessory Fe-Ti oxides in igneous rocks (Buddington and Lindsley, 1964; Frost and Lindsley, 1991; Liu et al., 2015; Tan et al., 2016b). High-Ti magnetite with oscillatory zoning in sample 084 cannot be explained as magmatic origin because it is commonly associated with hydrothermal mineral actinolite and lack of regular exsolution lamellae of Fe-Ti oxides. Low-Ti magnetite from sample 080 (Mag-2) overgrowing on the Mag-1 crystallized from a later moderate- to high-temperature magmatic-hydrothermal fluid (Fig. 13A). The decreasing Ti+V contents but constant V contents from Mag-1 in sample 080 and Mag-1D and Mag-1L in sample 084 to Mag-2 in samples 080 and 084 (Figs. 9A-B, 13A) indicate decreased temperature (e.g., from >500ºC to 300-500ºC) and relatively stable oxygen fugacity. This indicates that magnetite in some IOCG deposits has formed by both magmatic and magmatic-hydrothermal processes. This conclusion is supported by the features of two different orebodies in the Sossego deposit. The SPB orebodies in the deeper portion of the deposit are characterized by magnetite-(apatite) and albite-actinolite-rich zones, whereas the SC orebodies in shallower portion have predominant potassic and chlorite alteration

typical of shallow crustal levels (Monteiro et al., 2008a). The temperatures for Na-Ca alteration and ore stage in SPB orebodies are >500ºC and ~400ºC, respectively, whereas those for K-Fe alteration and ore stage in SC orebodies are ~400ºC and ~275ºC, respectively (Moreto et al., 2015). The texture and chemical composition of magnetite in the SC orebodies thus record the evolution of fluids from higher temperature magmatic or to lower temperature magmatic-hydrothermal stages in the Sossego deposit.

Magnetite from the El Romeral IOA deposit contains inclusion-rich cores (Mag-1) overgrown by inclusion-poor rims (Mag-2) which was further replaced by a trace element-rich magnetite (Mag-3). Mag-1 can be interpreted as igneous core observed in IOA magnetite from Missouri (Nold et al., 2014) and the Chilean Iron Belt (Knipping et al., 2015a, b; Rojas et al., 2018) because the regular distribution of Fe-Al oxides/Ti oxides and gangue minerals in the core (Figs. 3D, 7A) that indicates an exsolution process probably related to a magmatic event (Rojas et al., 2018). Both Mag-1 and Mag-2 have Ca+Al+Mn and Ti+V contents comparable with those from Kiruna-type IOA deposits (Fig. 13B). The differences in composition between Mag-1 and Mag-2 may be due to changing composition in fluids (Fig. 13B) rather than variations in temperature and oxygen fugacity in terms of similar Ti and V contents (Fig. 9B). Mag-3 has formed by replacement of Mag-2 via type 2 CDR process, the fluids responsible for Mag-3 are high-temperature magmatic-hydrothermal fluids similar in porphyry Cu deposits (Fig. 13B). Our magnetite generations and origins are consistent with the study of Rojas et al. (2018) where three generations of magnetite

were identified in El Romeral. Zoned magnetite grains with inclusion-rich cores and inclusion-poor rims (first and second generations) form the massive magnetite orebody, representing the main mineralization event. This main magnetite stage was followed by late hydrothermal events that are represented by magnetite veinlets (third generation) that crosscut the massive orebody. The first and second generations of magnetite were considered to be sourced from intermediate magmas, whereas the third generation of magnetite was formed by magmatic-hydrothermal fluids related to post-ore dioritic dikes (Rojas et al., 2018).

A similar scenario is also proposed for the Los Colorados IOA deposit in the Chilean iron belt where three generations of magnetite show chemical compositions changing from purely magmatic to magmatic-hydrothermal (Knipping et al., 2015a, b; Simon et al., 2018). Based on trace element and Fe-O isotope compositions of magnetite, Knipping et al. (2015a) proposed a model for IOA formation by flotation of magmatic magnetite suspensions to explain the variation in chemical composition of magnetite. Identification of igneous/magmatic magnetite in the Sossego IOCG deposit and El Romeral IOA deposit indicates that some IOCG deposits may have experienced similar process to IOA deposits where original Fe was derived from magmatic process, cf. either through magnetite flotation processes (Knipping et al., 2015a, b) or crystallization from Fe-rich melt (25-32 wt% FeO; 38-42 wt% SiO_2) separated from Si-rich melt (60-70 wt% SiO_2) by liquid immiscibility (Roedder and Weiblen, 1970; De, 1974; Dixon and Rutherford, 1979; Philpotts, 1982; Jakobsen et al., 2005; Hou et al., 2018). There are other examples that support a magmatic source

for ore-forming fluids in IOCG and Kiruna-type IOA deposits from Missouri IOA (USA), Kiruna IOA (Sweden), and Olympic Dam IOCG (Australia) districts (Simon et al., 2018). For example, Hofstra et al. (2016) concluded that a magmatic-hydrothermal ore fluid evolved from a concealed mafic to intermediate-composition magma was responsible for mineralization at the Pea Ridge IOA deposit in Missouri, based on mineral thermometry and fluid inclusion studies. Iron and oxygen stable isotope data of magnetite from the Pea Ridge and Pilot Knob IOA deposits in Missouri further indicated that magnetite crystallized from a silicate melt and grew in equilibrium with a magmatic-hydrothermal aqueous fluid (Childress et al., 2016). Wawryk (2017) reported Fe isotope data for samples from the Olympic Dam IOCG system that supports a magmatic source for Fe and, by inference, the ore-forming fluid that transported Fe and other metals and S. Moreover, deep drill core (end at ~2,329 m) at Olympic Dam revealed the presence of abundant, early magnetite and apatite at the deepest level of the mineralized system (Apukhtina et al., 2017). The magnetite-fluorapatite mineralization, resembling those characteristic of iron oxide-apatite deposits, extends more than 800 m (from 1,516 to 2,329 m) and likely continues beneath the bottom of the drill hole (Apukhtina et al., 2017). Therefore, we suggest that similar magmatic and magmatic-hydrothermal sources for ore-forming fluids link IOCG deposits with Kiruna-type IOA deposits.

Implication for deposit type discrimination diagrams

Different diagrams based on trace element composition of magnetite have been

proposed to discriminate magnetite from different types of deposits. These discrimination diagrams are used here to illustrate the compositional modification of magnetite during reequilibration processes and their applicability for provenance studies.

Dupuis and Beaudoin (2011) proposed the Ca+Al+Mn vs. Ti+V and Ni/(Cr+Mn) vs. Ti+V diagrams to discriminate IOCG and IOA deposits from Fe-Ti-V, porphyry, skarn deposits, and BIF. In these diagrams, iron oxides from IOCG deposits can be separated from those from IOA deposits due to lower total Ti and V contents. These diagrams were constructed based on a three-step discrimination process. The first step is to discriminate Ni-Cu-PGE deposits from other deposit types using Ni+Cr vs. Si+Mg diagram, whereas the second step is to discriminate VMS deposits from other deposit types using Al/(Zn+Ca) vs. Cu/(Si+Ca) diagram. The third step is to discriminate remaining deposit types such as IOCG, IOA, Fe-Ti-V, porphyry, skarn, and BIF. Moreover, these diagrams were based on the average magnetite composition of deposits and showed the compositional variety in a deposit. Because most magnetite has Ni and Cr contents lower than their respective detection limits of 84 ppm and 47 ppm, the diagram of Ni/(Cr+Mn) vs. Ti+V was not evaluated. As shown in Fig. 13C, type 1 CDR process has resulted in lower Ca+Al+Mn contents in secondary magnetite than primary magnetite but Ti+V contents are relatively constant during this process. The primary magnetite (core) with skarn affinity in Igarapé Bahia and Candelaria IOCG deposits can be modified by type 1 CDR process to form secondary magnetite (rim) with IOCG affinity (Fig. 13C). Similarly, the primary

magnetite (core) with IOCG affinity in Alemao IOCG deposit can be modified to secondary magnetite (rim) with unknown origin (Fig. 13C). Type 2 CDR process is reverse to type 1 CDR process which results in increased Ca+Al+Mn contents (Fig. 13A, B). Primary magnetite with unknown origin in the Sossego IOCG deposit can be changed to secondary magnetite with Kiruna, IOCG, and porphyry affinity by type 2 CDR process (Fig. 13A). Primary magnetite with Kiruna affinity in the El Romeral IOA deposit can be modified to secondary magnetite with porphyry affinity (Fig. 13B). Hydrothermal-reequilibrated igneous magnetite in altered granitic plutons (Handan-Xingtai iron district, North China Craton) also shows a large compositional variation from magmatic Fe-Ti, V deposit to skarn, porphyry, and Kiruna deposits (Wen et al., 2017). Therefore, magnetite experienced CDR processes cannot be used to discriminate their origins in the Ca+Al+Mn vs. Ti+V diagram. The composition of magnetite is not obviously modified during recrystallization (Fig. 13D) and thus magnetite after recrystallization can be used provenance study.

Loberg and Horndahl (1983) proposed V vs. Ti, V vs. Ni+Co, V vs. Ni, V/Ti vs. Ni/Ti, and V/Fe vs. Ti/Fe diagrams to discriminate IOA deposits from magmatic Fe-Ti deposits and BIF (Fig. 14). Although these diagrams are constructed by bulk composition of iron ores, they are considered to be reliable in discriminating magnetite from the studied deposit types (Heidarian et al., 2016; Broughm et al., 2017). Different generations of magnetite in the same sample have indistinguishable V and Ni contents (Fig. 14A), but have variable Ti contents and V/Ti, Ni/Ti, V/Fe, and Ti/Fe ratios (Fig. 14B-D). Magnetite from the IOCG and IOA deposits plots in

the field of magnetite-apatite and titaniferous iron ores in the V-Ni diagram (Fig. 14A), and the field of magnetite-apatite ores in the V/Ti-Ni/Ti and V-Ti diagrams (Fig. 14B, C). Moreover, magnetite from the El Romeral IOA deposit plots in the field of Chadormalu IOA deposit (Central Iran) (Heidarian et al., 2016), but part of magnetite samples from the IOCG deposits overlap the field of Kiruna and Rektorn (Sweden), and El Laco (Chile) IOA deposits (Broughm et al., 2017) (Fig. 14A-C). Magnetite samples from El Romeral, Kiruna, Rektorn, and El Laco IOA deposits plot in the field of magnetite-apatite ores in the V/Fe vs. Ti/Fe diagram (Fig. 14D), whereas some magnetite samples from the IOCG deposits plot in the lower V/Fe values of BIF. This indicates that the above four discrimination diagrams are efficient in distinguishing IOA deposits from magmatic Fe-Ti deposits and BIF although magnetite has experienced reequilibration processes. But these diagrams fail to separate IOCG from IOA deposits and BIF.

Conclusions

Four types of textures have been identified in magnetite from IOCG and IOA deposits, including original oscillatory zoning and reequilibration textures such as extensive coupled dissolution and reprecipitation and less common oxy-exsolution and recrystallization. Single magnetite sample may have experienced one of these processes or all of them. The original oscillatory zoning was likely derived from the crystal growth during fluctuating fluid compositions rather than various temperature and oxygen fugacity. Two different types of CDR processes are identified according

to textures and chemical compositions of different generations of magnetite. Type 1 CDR process transforming Mag-1 to Mag-2 is extensive, whereas type 2 CDR process transforming Mag-2 to Mag-3 is local. During type 1 CDR process most minor and trace elements such as Si, K, Ca, Mg, Al, and Mn are expelled from magnetite while Fe contents increase, in contrast with type 2 CDR process. Type 1 CDR process is possibly induced by the changing fluid composition and/or decreasing temperature during progressive alteration and ore formation, whereas type 2 CDR process can be interpreted as post-ore replacement due to a new pulse of magmatic-hydrothermal fluids. Some magnetite grains in IOCG and IOA deposits may have formed by a similar process, i.e., transition from purely magmatic to magmatic-hydrothermal process. Magnetite in IOCG and IOA deposits is susceptible to textural and compositional reequilibration during high-temperature magmatic and magmatic-hydrothermal processes. The reequilibrated magnetite has textures and chemical compositions different from its precursor, complicating existing discrimination plots for genetic interpretation. This study highlights that understanding the ore genesis of IOCG and IOA deposits should combine magnetite chemistry with its textures.

Acknowledgments

This project was funded by China Scholarship Council (CSC, 201604910462), the Natural Science and Engineering Research Council (NSERC) of Canada, Agnico Eagle Mines Limited, and Ministère de l'Énergie et des Ressources Naturelles du

Québec within the NSERC-Agnico Eagle Industrial Research Chair in Mineral Exploration. We thank Maryse Henry (Geotop-UQAM) and Marc Choquette (Laval U.) for their assistance with SEM and EPMA analyses, respectively. Special thanks to Michel Jébrak (UQAM), Sarah Dare (U. of Ottawa), Lluis Fontboté (U. of Geneva), Isabelle McMartin (GSC), Roberto Perez Xavier (USP Säo Paulo), Robert Marschik (LMU Munich) and John Hanchar (Memorial U. of Newfoundland) who provided representative samples. Discussion with Louise Corriveau (Geological Survey of Canada) on the draft improved the understanding of IOCG and IOA ore formation. We acknowledge constructive reviews from Adam Simon and Artur Deditius, and editorial handling by Larry Meinert.

REFERENCES

Altree-Williams, A., Pring, A., Ngothai, Y., and Brugger, J., 2015, Textural and compositional complexities resulting from coupled dissolution–reprecipitation reactions in geomaterials: Earth-Science Reviews, v. 150, p. 628-651.

Apukhtina, O.B., Kamenetsky, V.S., Ehrig, K., Kamenetsky, M.B., Maas, R., Thompson, J., McPhie, J., Ciobanu, C.L., and Cook, N.J., 2017, Early, deep magnetite-fluorapatite mineralization at the Olympic Dam Cu-U-Au-Ag deposit, South Australia: Economic Geology, v. 112, p. 1531-1542.

Baker, T., Mustard, R., Fu, B., Williams, P.J., Dong, G., Fisher, L., Mark, G., and Ryan, C.G., 2008, Mixed messages in iron oxide–copper–gold systems of the Cloncurry district, Australia: insights from PIXE analysis of halogens and copper in

fluid inclusions: Mineralium Deposita, v. 43, p. 599-608.

Barton, M.D., and Johnson, D.A., 1996, Evaporitic-source model for igneous-related Fe oxide–(REE-Cu-Au-U) mineralization: Geology, v. 24, p. 259-262.

Barton, M.D., and Johnson, D.A., 2000, Alternative brine sources for Fe-oxide (-Cu-Au) systems: Implications for hydrothermal alteration and metals, *in* Porter, T. M., ed., Hydrothermal iron oxide copper-gold and related deposits: a global perspective, 1: Adelaide, Australian Mineral Foundation, p. 43-60.

Barton, M.D., and Johnson, D.A., 2004, Footprints of Fe oxide (-Cu-Au) systems: University of Western Australia Special Publication, v. 33, p. 112-116.

Bookstrom, A.A., 1977, The magnetite deposits of El Romeral, Chile: Economic Geology, v. 72, p. 1101-1130.

Boutroy, E., Dare, S.A.S., Beaudoin, G., Barnes, S.-J., and Lightfoot, P.C., 2014, Magnetite composition in Ni-Cu-PGE deposits worldwide and its application to mineral exploration: Journal of Geochemical Exploration, v. 145, p. 64-81.

Broughm, S.G., Hanchar, J.M., Tornos, F., Westhues, A., and Attersley, S., 2017, Mineral chemistry of magnetite from magnetite-apatite mineralization and their host rocks: examples from Kiruna, Sweden, and El Laco, Chile: Mineralium Deposita, v. 52, p. 1223-1244.

Buddington, A., and Lindsley, D., 1964, Iron-titanium oxide minerals and synthetic equivalents: Journal of Petrology, v. 5, p. 310-357.

Chen, H., 2013, External sulphur in IOCG mineralization: Implications on definition and classification of the IOCG clan: Ore Geology Reviews, v. 51, p. 74-78.

Chen, W.T., Zhou, M.-F., Gao, J.-F., and Hu, R.Z., 2015, Geochemistry of magnetite from Proterozoic Fe-Cu deposits in the Kangdian metallogenic province, SW China: Mineralium Deposita, v. 50, p. 795-809.

Childress, T.M., Simon, A.C., Day, W.C., Lundstrom, C.C., and Bindeman, I.N., 2016, Iron and oxygen isotope signatures of the Pea Ridge and Pilot Knob magnetite-apatite deposits, southeast Missouri, USA: Economic Geology, v. 111, p. 2033-2044.

Chou, I.-M., and Eugster, H.P., 1977, Solubility of magnetite in supercritical chloride solutions: American Journal of Science, v. 277, p. 1296-1314.

Chu, X.L., and Ross, J., 1990, Complex kinetics of systems with multiple stationary states at equilibrium: The Journal of Chemical Physics, v. 93, p. 1613-1625.

Chung, D., Zhou, M.-F., Gao, J.-F., and Chen, W.T., 2015, In-situ LA–ICP-MS trace elemental analyses of magnetite: The late Palaeoproterozoic Sokoman Iron Formation in the Labrador Trough, Canada: Ore Geology Reviews, v. 65, p. 917-928.

Ciobanu, C.L., and Cook, N.J., 2004, Skarn textures and a case study: the Ocna de Fier-Dognecea orefield, Banat, Romania: Ore Geology Reviews, v. 24, p. 315-370.

Corriveau, L., Montreuil, J.-F., and Potter, E., 2016, Alteration facies linkages among iron oxide copper-gold, iron oxide-apatite, and affiliated deposits in the Great Bear magmatic zone, Northwest Territories, Canada: Economic Geology, v. 111, p. 2045-2072.

Corriveau, L., Ootes, L., Mumin, H., Jackson, V., Bennett, V., Cremer, J.F., Rivard, B.,

McMartin, I., and Beaudoin, G., 2007, Alteration vectoring to IOCG(U) deposits in frontier volcano-plutonic terrains, Canada, *in* Milkereit, B., ed., Proceedings of Exploration 07: Fifth Decennial International Conference on Mineral Exploration, p. 1171-1177.

Daliran, F., Stosch, H.G., Williams, P.J., Jamali, H., and Dorri, M.B., 2010, Early-Cambrian iron oxide-apatite-REE (U) deposits of the Bafq district, east-central Iran, *in* Corriveau, L., and Mumin, H., eds., Exploring for iron oxide copper-gold deposits: Canada and global analogues, Geological Association of Canada, Short Course Notes 20, p. 147-159.

Dare, S.A., Barnes, S.-J., and Beaudoin, G., 2015, Did the massive magnetite "lava flows" of El Laco (Chile) form by magmatic or hydrothermal processes? New constraints from magnetite composition by LA-ICP-MS: Mineralium Deposita, v. 50, p. 607-617.

Dare, S.A.S., Barnes, S.-J., and Beaudoin, G., 2012, Variation in trace element content of magnetite crystallized from a fractionating sulfide liquid, Sudbury, Canada: Implications for provenance discrimination: Geochimica et Cosmochimica Acta, v. 88, p. 27-50.

Dare, S.A.S., Barnes, S.-J., Beaudoin, G., Méric, J., Boutroy, E., and Potvin-Doucet, C., 2014, Trace elements in magnetite as petrogenetic indicators: Mineralium Deposita, v. 49, p. 785-796.

De, A., 1974, Silicate liquid immiscibility in the Deccan Traps and its petrogenetic significance: Geological Society of America Bulletin, v. 85, p. 471-474.

Deditius, A.P., Reich, M., Simon, A.C., Suvorova, A., Knipping, J., Roberts, M.P., Rubanov, S., Dodd, A., and Saunders, M., 2018, Nanogeochemistry of hydrothermal magnetite: Contributions to Mineralogy and Petrology, v. 173, p. 46.

deMelo, G.H.C., Monteiro, L.V.S., Xavier, R.P., Moreto, C.P.N., Santiago, E.S.B., Dufrane, S.A., Aires, B., and Santos, A.F.F., 2017, Temporal evolution of the giant Salobo IOCG deposit, Carajás Province (Brazil): constraints from paragenesis of hydrothermal alteration and U-Pb geochronology: Mineralium Deposita, v. 52, p. 709-732.

Dixon, S., and Rutherford, M.J., 1979, Plagiogranites as late-stage immiscible liquids in ophiolite and mid-ocean ridge suites: an experimental study: Earth and Planetary Science Letters, v. 45, p. 45-60.

Dreher, A.M., Xavier, R.P., Taylor, B.E., and Martini, S.L., 2008, New geologic, fluid inclusion and stable isotope studies on the controversial Igarapé Bahia Cu–Au deposit, Carajás Province, Brazil: Mineralium Deposita, v. 43, p. 161-184.

Dupuis, C., and Beaudoin, G., 2011, Discriminant diagrams for iron oxide trace element fingerprinting of mineral deposit types: Mineralium Deposita, v. 46, p. 1-17.

Edfelt, Å., Armstrong, R.N., Smith, M., and Martinsson, O., 2005, Alteration paragenesis and mineral chemistry of the Tjårrojåkka apatite–iron and Cu (-Au) occurrences, Kiruna area, northern Sweden: Mineralium Deposita, v. 40, p. 409-434.

Foerster, H., and Jafarzadeh, A., 1994, The Bafq mining district in central Iran; a

highly mineralized Infracambrian volcanic field: Economic Geology, v. 89, p. 1697-1721.

Frietsch, R., and Perdahl, J.-A., 1995, Rare earth elements in apatite and magnetite in Kiruna-type iron ores and some other iron ore types: Ore Geology Reviews, v. 9, p. 489-510.

Frost, B.R., 1991, Introduction to oxygen fugacity and its petrologic importance, *in* Lindsley, D. H., ed., Oxide minerals: petrologic and magnetic significance, 25, Reviews in Mineralogy and Geochemistry, p. 1-9.

Frost, B.R., and Lindsley, D.H., 1991, Occurrence of iron-titanium oxides in igneous rocks, *in* Lindsley, D. H., ed., Oxide minerals: petrologic and magnetic significance, 25, Reviews in Mineralogy and Geochemistry, p. 433-468.

Grigsby, J.D., 1990, Detrital magnetite as a provenance indicator: Journal of Sedimentary Research, v. 60, p. 940-951.

Groves, D.I., Bierlein, F.P., Meinert, L.D., and Hitzman, M.W., 2010, Iron oxide copper-gold (IOCG) deposits through Earth history: Implications for origin, lithospheric setting, and distinction from other epigenetic iron oxide deposits: Economic Geology, v. 105, p. 641-654.

Harlov, D.E., 1992, Comparative oxygen barometry in granulites, Bamble Sector, SE Norway: The Journal of Geology, v. 100, p. 447-464.

Harlov, D.E., and Hansen, E.C., 2005, Oxide and sulphide isograds along a Late Archean, deep - crustal profile in Tamil Nadu, south India: Journal of Metamorphic Geology, v. 23, p. 241-259.

Harlov, D.E., Wirth, R., and Förster, H.-J., 2005, An experimental study of dissolution–reprecipitation in fluorapatite: fluid infiltration and the formation of monazite: Contributions to Mineralogy and Petrology, v. 150, p. 268-286.

Harlov, D.E., Wirth, R., and Hetherington, C.J., 2011, Fluid-mediated partial alteration in monazite: the role of coupled dissolution–reprecipitation in element redistribution and mass transfer: Contributions to Mineralogy and Petrology, v. 162, p. 329-348.

Haynes, D.W., Cross, K.C., Bills, R.T., and Reed, M.H., 1995, Olympic Dam ore genesis: a fluid-mixing model: Economic Geology, v. 90, p. 281-307.

Heidarian, H., Lentz, D., Alirezaei, S., Peighambari, S., and Hall, D., 2016, Using the chemical analysis of magnetite to constrain various stages in the formation and genesis of the Kiruna-type chadormalu magnetite-apatite deposit, Bafq district, Central Iran: Mineralogy and Petrology, v. 110, p. 927-942.

Hellmann, R., Wirth, R., Daval, D., Barnes, J.-P., Penisson, J.-M., Tisserand, D., Epicier, T., Florin, B., and Hervig, R.L., 2012, Unifying natural and laboratory chemical weathering with interfacial dissolution–reprecipitation: a study based on the nanometer-scale chemistry of fluid–silicate interfaces: Chemical Geology, v. 294, p. 203-216.

Henríquez, F., Naslund, H.R., Nyström, J.O., Vivallo, W., Aguirre, R., Dobbs, F.M., and Lledó, H., 2003, New field evidence bearing on the origin of the El Laco magnetite deposit, northern Chile—a discussion: Economic Geology, v. 98, p. 1497-1500.

Henríquez, F., and Nyström, J.O., 1998, Magnetite bombs at El Laco volcano, Chile: GFF, v. 120, p. 269-271.

Hitzman, M.W., 2000, Iron oxide-Cu-Au deposits: what, where, when, and why, *in* Porter, T. M., ed., Hydrothermal iron oxide copper-gold & related deposits: a global perspective, 1: Adelaide, PGC Publishing, p. 9-25.

Hitzman, M.W., Oreskes, N., and Einaudi, M.T., 1992, Geological characteristics and tectonic setting of Proterozoic iron oxide (Cu ± U ± Au ± REE) deposits: Precambrian Research, v. 58, p. 241-287.

Hjelmfelt, A., and Ross, J., 1991, Experiments on an oscillatory system close to equilibrium: The Journal of Chemical Physics, v. 94, p. 5999-6002.

Hofstra, A.H., Meighan, C.J., Song, X., Samson, I., Marsh, E.E., Lowers, H.A., Emsbo, P., and Hunt, A.G., 2016, Mineral thermometry and fluid inclusion studies of the Pea Ridge iron oxide-apatite–rare earth element deposit, Mesoproterozoic St. Francois Mountains terrane, southeast Missouri, USA: Economic Geology, v. 111, p. 1985-2016.

Holten, T., Jamtveit, B., and Meakin, P., 2000, Noise and oscillatory zoning of minerals: Geochimica et Cosmochimica Acta, v. 64, p. 1893-1904.

Hoskin, P.W.O., and Black, L.P., 2000, Metamorphic zircon formation by solid‐state recrystallization of protolith igneous zircon: Journal of metamorphic Geology, v. 18, p. 423-439.

Hou, T., Charlier, B., Holtz, F., Veksler, I., Zhang, Z., Thomas, R., and Namur, O., 2018, Immiscible hydrous Fe–Ca–P melt and the origin of iron oxide-apatite ore

deposits: Nature Communications, v. 9, p. 1415.

Hu, H., Lentz, D., Li, J.-W., McCarron, T., Zhao, X.-F., and Hall, D., 2015, Reequilibration processes in magnetite from iron skarn deposits: Economic Geology, v. 110, p. 1-8.

Hu, H., Li, J.-W., Lentz, D., Ren, Z., Zhao, X.-F., Deng, X.-D., and Hall, D., 2014, Dissolution–reprecipitation process of magnetite from the Chengchao iron deposit: Insights into ore genesis and implication for *in-situ* chemical analysis of magnetite: Ore Geology Reviews, v. 57, p. 393-405.

Huang, X.-W., Boutroy, É., Makvandi, S., Beaudoin, G., Corriveau, L., and De Toni, A.F., 2019, Trace element composition of iron oxides from IOCG and IOA deposits: relationship to hydrothermal alteration and deposit subtypes: Mineralium Deposita, v. 54, p. 525-552.

Huang, X.-W., Boutry, E., Beaudoin, G., Makvandi, S., Corriveau, L., and De Toni, A.F., 2017, Trace element composition of iron oxides from IOCG and IOA deposits, and relationships to hydrothermal alteration and deposit subtypes: Proceedings of the 14th SGA Biennial Meeting, 20-23 August 2017, Quebec city, 2017, p. 931-934.

Huang, X.-W., Gao, J.-F., Qi, L., Meng, Y.-M., Wang, Y.-C., and Dai, Z.-H., 2016, In-situ LA-ICP-MS trace elements analysis of magnetite: The Fenghuangshan Cu-Fe-Au deposit, Tongling, Eastern China: Ore Geology Reviews, v. 72, p. 746-759.

Huang, X.-W., Gao, J.-F., Qi, L., and Zhou, M.-F., 2015a, In-situ LA-ICP-MS trace

elemental analyses of magnetite and Re–Os dating of pyrite: The Tianhu hydrothermally remobilized sedimentary Fe deposit, NW China: Ore Geology Reviews, v. 65, p. 900-916.

Huang, X.-W., Qi, L., and Meng, Y.-M., 2014, Trace element geochemistry of magnetite from the Fe(-Cu) deposits in the Hami region, Eastern Tianshan Orogenic Belt, NW China: Acta Geologica Sinica, v. 88, p. 176-195.

Huang, X.-W., Zhou, M.-F., Beaudoin, G., Gao, J.-F., Qi, L., and Lyu, C., 2018, Origin of the volcanic-hosted Yamansu Fe deposit, Eastern Tianshan, NW China: constraints from pyrite Re-Os isotopes, stable isotopes, and in situ magnetite trace elements: Mineralium Deposita, v. 53, p. 1039-1060.

Huang, X.-W., Zhou, M.-F., Qi, L., Gao, J.-F., and Wang, Y.-W., 2013, Re-Os isotopic ages of pyrite and chemical composition of magnetite from the Cihai magmatic-hydrothermal Fe deposit, NW China: Mineralium Deposita, v. 48, p. 925-946.

Huang, X.-W., Zhou, M.-F., Qiu, Y.-Z., and Qi, L., 2015b, In-situ LA-ICP-MS trace elemental analyses of magnetite: The Bayan Obo Fe-REE-Nb deposit, North China: Ore Geology Reviews, v. 65, p. 884-899.

Ilton, E.S., and Eugster, H.P., 1989, Base metal exchange between magnetite and a chloride-rich hydrothermal fluid: Geochimica et Cosmochimica Acta, v. 53, p. 291-301.

Jakobsen, J.K., Veksler, I.V., Tegner, C., and Brooks, C.K., 2005, Immiscible iron-and silica-rich melts in basalt petrogenesis documented in the Skaergaard intrusion:

Geology, v. 33, p. 885-888.

Jarosewich, E., Nelen, J., and Norberg, J.A., 1980, Reference samples for electron microprobe analysis: Geostandards Newsletter, v. 4, p. 43-47.

Kendrick, M., Baker, T., Fu, B., Phillips, D., and Williams, P., 2008, Noble gas and halogen constraints on regionally extensive mid-crustal Na–Ca metasomatism, the Proterozoic Eastern Mount Isa Block, Australia: Precambrian Research, v. 163, p. 131-150.

Kendrick, M., Mark, G., and Phillips, D., 2007, Mid-crustal fluid mixing in a Proterozoic Fe oxide–Cu–Au deposit, Ernest Henry, Australia: evidence from Ar, Kr, Xe, Cl, Br, and I: Earth and Planetary Science Letters, v. 256, p. 328-343.

Knipping, J.L., Bilenker, L.D., Simon, A.C., Reich, M., Barra, F., Deditius, A.P., Lundstrom, C., Bindeman, I., and Munizaga, R., 2015a, Giant Kiruna-type deposits form by efficient flotation of magmatic magnetite suspensions: Geology, v. 43, p. 591-594.

Knipping, J.L., Bilenker, L.D., Simon, A.C., Reich, M., Barra, F., Deditius, A.P., Wälle, M., Heinrich, C.A., Holtz, F., and Munizaga, R., 2015b, Trace elements in magnetite from massive iron oxide-apatite deposits indicate a combined formation by igneous and magmatic-hydrothermal processes: Geochimica et Cosmochimica Acta, v. 171, p. 15-38.

Lindenmayer, Z.G., and Teixeira, J.B.G., 1999, Ore genesis at the Salobo copper deposit, Serra dos Carajás, *in* Silva, M. G., and Misi, A., eds., Base metal deposits of Brazil, MME/CPRM/DNPM, p. 33-43.

Lindsley, D.H., 1991, Experimental studies of oxide minerals: Reviews in Mineralogy and Geochemistry, v. 25, p. 69-106.

Liu, P.-P., Zhou, M.-F., Chen, W.T., Gao, J.-F., and Huang, X.-W., 2015, In-situ LA-ICP-MS trace elemental analyses of magnetite: Fe–Ti–(V) oxide-bearing mafic–ultramafic layered intrusions of the Emeishan Large Igneous Province, SW China: Ore Geology Reviews, v. 65, p. 853-871.

Loberg, B.E.H., and Horndahl, A.K., 1983, Ferride geochemistry of Swedish Precambrian iron ores: Mineralium Deposita, v. 18, p. 487-504.

Mücke, A., and Younessi, R., 1994, Magnetite-apatite deposits (Kiruna-type) along the Sanandaj-Sirjan zone and in the Bafq area, Iran, associated with ultramafic and calcalkaline rocks and carbonatites: Mineralogy and Petrology, v. 50, p. 219-244.

Makvandi, S., Beaudoin, G., McClenaghan, B.M., and Layton-Matthews, D., 2015, The surface texture and morphology of magnetite from the Izok Lake volcanogenic massive sulfide deposit and local glacial sediments, Nunavut, Canada: Application to mineral exploration: Journal of Geochemical Exploration, v. 150, p. 84-103.

Makvandi, S., Ghasemzadeh-Barvarz, M., Beaudoin, G., Grunsky, E.C., McClenaghan, M.B., and Duchesne, C., 2016a, Principal component analysis of magnetite composition from volcanogenic massive sulfide deposits: Case studies from the Izok Lake (Nunavut, Canada) and Halfmile Lake (New Brunswick, Canada) deposits: Ore Geology Reviews, v. 72, p. 60-85.

Makvandi, S., Ghasemzadeh-Barvarz, M., Beaudoin, G., Grunsky, E.C., McClenaghan, M.B., Duchesne, C., and Boutroy, E., 2016b, Partial least

squares-discriminant analysis of trace element compositions of magnetite from various VMS deposit subtypes: Application to mineral exploration: Ore Geology Reviews, v. 78, p. 388-408.

Marschik, R., Chiaradia, M., and Fontboté, L., 2003, Implications of Pb isotope signatures of rocks and iron oxide Cu-Au ores in the Candelaria-Punta del Cobre district, Chile: Mineralium Deposita, v. 38, p. 900-912.

Marschik, R., and Fontboté, L., 2001, The Candelaria-Punta del Cobre iron oxide Cu-Au (-Zn-Ag) deposits, Chile: Economic Geology, v. 96, p. 1799-1826.

Mathur, R., Marschik, R., Ruiz, J., Munizaga, F., Leveille, R.A., and Martin, W., 2002, Age of mineralization of the Candelaria Fe oxide Cu-Au deposit and the origin of the Chilean iron belt, based on Re-Os isotopes: Economic Geology, v. 97, p. 59-71.

Meinert, L.D., Dipple, G.M., and Nicolescu, S., 2005, World skarn deposits, *in* Hedenquist, J. W., Thompson, J. F. H., Goldfarb, R. J., and Richards, J. P., eds., Economic Geology 100th Anniversary Volume: Littleton, Colorado, Society of Economic Geologists, p. 299-336.

Monteiro, L.V.S., Xavier, R.P., De Carvalho, E.R., Hitzman, M.W., Johnson, C.A., De Souza Filho, C.R., and Torresi, I., 2008a, Spatial and temporal zoning of hydrothermal alteration and mineralization in the Sossego iron oxide–copper–gold deposit, Carajás Mineral Province, Brazil: paragenesis and stable isotope constraints: Mineralium Deposita, v. 43, p. 129-159.

Monteiro, L.V.S., Xavier, R.P., Hitzman, M.W., Juliani, C., De Souza Filho, C.R., and Carvalho, E.d.R., 2008b, Mineral chemistry of ore and hydrothermal alteration at

the Sossego iron oxide–copper–gold deposit, Carajás Mineral Province, Brazil: Ore Geology Reviews, v. 34, p. 317-336.

Moreto, C.P.N., Monteiro, L.V.S., Xavier, R.P., Creaser, R.A., DuFrane, S.A., Tassinari, C.C.G., Sato, K., Kemp, A.I.S., and Amaral, W.S., 2015, Neoarchean and Paleoproterozoic iron oxide-copper-gold events at the Sossego Deposit, Carajás Province, Brazil: Re-Os and U-Pb geochronological evidence: Economic Geology, v. 110, p. 809-835.

Nadoll, P., Angerer, T., Mauk, J.L., French, D., and Walshe, J., 2014, The chemistry of hydrothermal magnetite: A review: Ore Geology Reviews, v. 61, p. 1-32.

Nadoll, P., Mauk, J.L., Leveille, R.A., and Koenig, A.E., 2015, Geochemistry of magnetite from porphyry Cu and skarn deposits in the southwestern United States: Mineralium Deposita, v. 50, p. 493-515.

Naslund, H.R., Henríquez, F., Nyström, J.O., Vivallo, W., and Dobbs, F.M., 2002, Magmatic iron ores and associated mineralization: Examples from the Chilean high Andes and coastal Cordillera, *in* Porter, T. M., ed., Hydrothermal iron oxide copper-gold and related deposits: A global perspective, 2: Adelaide, PGC Publishing, p. 207-226.

Neumann, E.-R., Svensen, H.H., Polozov, A.G., and Hammer, Ø., 2017, Formation of Si-Al-Mg-Ca-rich zoned magnetite in an end-Permian phreatomagmatic pipe in the Tunguska Basin, East Siberia: Mineralium Deposita, v. 52, p. 1205-1222.

Niedermeier, D.R.D., Putnis, A., Geisler, T., Golla-Schindler, U., and Putnis, C.V., 2009, The mechanism of cation and oxygen isotope exchange in alkali feldspars

under hydrothermal conditions: Contributions to Mineralogy and Petrology, v. 157, p. 65-76.

Nold, J.L., Davidson, P., and Dudley, M.A., 2013, The pilot knob magnetite deposit in the Proterozoic St. Francois Mountains Terrane, southeast Missouri, USA: A magmatic and hydrothermal replacement iron deposit: Ore Geology Reviews, v. 53, p. 446-469.

Nold, J.L., Dudley, M.A., and Davidson, P., 2014, The Southeast Missouri (USA) Proterozoic iron metallogenic province—Types of deposits and genetic relationships to magnetite–apatite and iron oxide–copper–gold deposits: Ore Geology Reviews, v. 57, p. 154-171.

Nyström, J.O., and Henríquez, F., 1994, Magmatic features of iron ores of the Kiruna type in Chile and Sweden; ore textures and magnetite geochemistry: Economic Geology, v. 89, p. 820-839.

Ortoleva, P., Merino, E., Moore, C., and Chadam, J., 1987, Geochemical self-organization I: reaction-transport feedbacks and modeling approach: American Journal of Science, v. 287, p. 979-1007.

Philpotts, A.R., 1982, Compositions of immiscible liquids in volcanic rocks: Contributions to Mineralogy and Petrology, v. 80, p. 201-218.

Pisiak, L.K., Canil, D., Lacourse, T., Plouffe, A., and Ferbey, T., 2017, Magnetite as an indicator mineral in the exploration of porphyry deposits: A case study in till near the Mount Polley Cu-Au deposit, British Columbia, Canada: Economic Geology, v. 112, p. 919-940.

Pollard, P.J., 2000, Evidence of a magmatic fluid and metal source for Fe-oxide Cu-Au mineralization, *in* Porter, T. M., ed., Hydrothermal iron oxide copper-gold and related deposits: a global perspective: Adelaide, Australian Mineral Foundation, p. 27-41.

Pollok, K., Putnis, C.V., and Putnis, A., 2011, Mineral replacement reactions in solid solution-aqueous solution systems: Volume changes, reactions paths and end-points using the example of model salt systems: American Journal of Science, v. 311, p. 211-236.

Putnis, A., 1992, An introduction to mineral sciences: Cambridge, Cambridge University Press.

Putnis, A., 2002, Mineral replacement reactions: from macroscopic observations to microscopic mechanisms: Mineralogical Magazine, v. 66, p. 689-708.

Putnis, A., 2009, Mineral replacement reactions: Reviews in Mineralogy and Geochemistry, v. 70, p. 87-124.

Putnis, A., 2015, Transient porosity resulting from fluid–mineral interaction and its consequences: Rev Mineral Geochem, v. 80, p. 1-23.

Putnis, A., and Austrheim, H., 2013, Mechanisms of metasomatism and metamorphism on the local mineral scale: the role of dissolution-reprecipitation during mineral re-equilibration, *in* Harlov, D. E., and Austrheim, H., eds., Metasomatism and the chemical transformation of rock: The role of fluids in terrestrial and extraterrestrial processes: Berlin-Heidelberg, Springer-Verlag, p. 141-170.

Putnis, A., Fernandez-Diaz, L., and Prieto, M., 1992, Experimentally produced oscillatory zoning in the (Ba, Sr)SO_4 solid solution: Nature, v. 358, p. 743-745.

Putnis, A., and John, T., 2010, Replacement processes in the Earth's crust: Elements, v. 6, p. 159-164.

Putnis, A., and Putnis, C.V., 2007, The mechanism of reequilibration of solids in the presence of a fluid phase: Journal of Solid State Chemistry, v. 180, p. 1783-1786.

Putnis, C.V., Tsukamoto, K., and Nishimura, Y., 2005, Direct observations of pseudomorphism: compositional and textural evolution at a fluid-solid interface: American Mineralogist, v. 90, p. 1909-1912.

Réquia, K.C.M., and Xavier, R.P., 1995, Fases fluidas na evolução metamórfica do depósito de Cu-Au de Salobo, Carajás, Pará: Revista da Escola de Minas, v. 49, p. 117-122.

Requia, K., 2002, The Archean Salobo iron oxide copper–gold deposit, Carajás Mineral Province, Brazil: Unpub. PhD Thesis thesis, University of Geneva.

Requia, K., and Fontboté, L., 2000, The Salobo iron oxide copper-gold deposit, Carajás, northern Brazil, *in* Porter, T. M., ed., Hydrothermal iron-oxide copper-gold and related deposits: a global perspective, 1: Adelaide, PGC Publishing, p. 225-236.

Requia, K., Stein, H., Fontboté, L., and Chiaradia, M., 2003, Re–Os and Pb–Pb geochronology of the Archean Salobo iron oxide copper–gold deposit, Carajás mineral province, northern Brazil: Mineralium Deposita, v. 38, p. 727-738.

Rhodes, A.L., Oreskes, N., and Sheets, S.A., 1999, Geology and rare earth element (REE) geochemistry of magnetite deposits at El Laco, Chile, *in* Skinner, B. J., ed.,

Geology and ore deposits of the Central Andes, Society of Economic Geologists Special Publication 7, p. 299-332.

Roedder, E., and Weiblen, P.W., 1970, Silicate liquid immiscibility in lunar magmas, evidenced by melt inclusions in lunar rocks: Science, v. 167, p. 641-644.

Rojas, P.A., Barra, F., Reich, M., Deditius, A., Simon, A., Uribe, F., Romero, R., and Rojo, M., 2018, A genetic link between magnetite mineralization and diorite intrusion at the El Romeral iron oxide-apatite deposit, northern Chile: Mineralium Deposita, v. 53, p. 947-966.

Ronzê, P.C., Soares, A.D.V., dos Santos, M.G.S., and Barreira, C.F., 2000, Alemão copper-gold (U-REE) deposit, Carajás, Brazil, *in* Poter, T. M., ed., Hydrothermal iron oxide copper-gold & related deposits: a global perspective, 1: Adelaide, PGC Publishing, p. 191-202.

Ruiz-Agudo, E., Putnis, C.V., and Putnis, A., 2014, Coupled dissolution and precipitation at mineral–fluid interfaces: Chemical Geology, v. 383, p. 132-146.

Sappin, A.-A., Dupuis, C., Beaudoin, G., Pozza, M., McMartin, I., and McClenaghan, M., 2014, Optimal ferromagnetic fraction in till samples along ice-flow paths: case studies from the Sue-Dianne and Thompson deposits, Canada: Geochemistry: Exploration, Environment, Analysis, v. 14, p. 315-329.

Shimazaki, H., 1998, On the occurrence of silician magnetites: Resource Geology, v. 48, p. 23-29.

Shore, M., and Fowler, A.D., 1996, Oscillatory zoning in minerals: a common phenomenon: The Canadian Mineralogist, v. 34, p. 1111-1126.

Sievwright, R.H., Wilkinson, J.J., O'Neill, H.S.C., and Berry, A.J., 2017, Thermodynamic controls on element partitioning between titanomagnetite and andesitic–dacitic silicate melts: Contributions to Mineralogy and Petrology, v. 172, p. 1-33.

Sillitoe, R.H., 2003, Iron oxide-copper-gold deposits: an Andean view: Mineralium Deposita, v. 38, p. 787-812.

Sillitoe, R.H., and Burrows, D.R., 2002, New field evidence bearing on the origin of the El Laco magnetite deposit, northern Chile: Economic Geology, v. 97, p. 1101-1109.

Simon, A.C., Knipping, J., Reich, M., Barra, F., Deditius, A.P., Bilenker, L., and Childress, T., 2018, Kiruna-Type Iron Oxide-Apatite (IOA) and Iron Oxide Copper-Gold (IOCG) Deposits Form by a Combination of Igneous and Magmatic-Hydrothermal Processes: Evidence from the Chilean Iron Belt: Economic Geology Special Publications, v. 21, p. 89-114.

Simon, A.C., Pettke, T., Candela, P.A., Piccoli, P.M., and Heinrich, C.A., 2004, Magnetite solubility and iron transport in magmatic-hydrothermal environments: Geochimica et Cosmochimica Acta, v. 68, p. 4905-4914.

Singoyi, B., Danyushevsky, L., Davidson, G.J., Large, R., and Zaw, K., 2006, Determination of trace elements in magnetites from hydrothermal deposits using the LA ICP-MS technique: SEG Keystone Conference, Denver, USA, CD-ROM, 2006.

Tallarico, F.H., Figueiredo, B.R., Groves, D.I., Kositcin, N., McNaughton, N.J.,

Fletcher, I.R., and Rego, J.L., 2005, Geology and SHRIMP U-Pb geochronology of the Igarapé Bahia deposit, Carajás copper-gold belt, Brazil: an archean (2.57 Ga) example of iron-oxide Cu-Au-(U-REE) mineralization: Economic Geology, v. 100, p. 7-28.

Tan, W., He, H., Wang, C.Y., Dong, H., Liang, X., and Zhu, J., 2016a, Magnetite exsolution in ilmenite from the Fe-Ti oxide gabbro in the Xinjie intrusion (SW China) and sources of unusually strong remnant magnetization: American Mineralogist, v. 101, p. 2759-2767.

Tan, W., Wang, C.Y., He, H.P., Liang, X.L., and Liu, P., 2016b, Mineralogy and origin of exsolution in Ti-rich magnetite from different magmatic Fe-Ti oxide-bearing intrusions: The Canadian Mineralogist, v. 54, p. 539-553.

Tazava, E., and De Oliveira, C.G., 2000, The Igarapé Bahia Au-Cu-(REE-U) deposit, Carajás Mineral Province, Northern Brazil, *in* Poter, T. M., ed., Hydrothermal iron oxide copper–gold & related deposits: a global perspective, 1: Adelaide, PGC Publishing, p. 203-212.

Toplis, M.J., and Corgne, A., 2002, An experimental study of element partitioning between magnetite, clinopyroxene and iron-bearing silicate liquids with particular emphasis on vanadium: Contributions to Mineralogy and Petrology, v. 144, p. 22-37.

Tornos, F., 2011, Magnetite-apatite and IOCG deposits formed by magmatic-hydrothermal evolution of complex calcalkaline melts: Proceedings of 11th Biennial SGA Meeting, 26-29 September 2011, Antofagasta, Chile, 2011, p.

443-445.

Tornos, F., Velasco, F., and Hanchar, J.M., 2016, Iron-rich melts, magmatic magnetite, and superheated hydrothermal systems: The El Laco deposit, Chile: Geology, v. 44, p. 427-430.

Urai, J.L., Means, W.D., and Lister, G.S., 1986, Dynamic recrystallization of minerals, *in* Hobbs, B. E., and Heard, H. C., eds., Mineral and rock deformation: laboratory studies: The Paterson volume, 36: Washington, D. C., American Geophysical Union, p. 161-199.

Valley, P.M., Fisher, C.M., Hanchar, J.M., Lam, R., and Tubrett, M., 2010, Hafnium isotopes in zircon: A tracer of fluid-rock interaction during magnetite–apatite ("Kiruna-type") mineralization: Chemical geology, v. 275, p. 208-220.

Velasco, F., Tornos, F., and Hanchar, J.M., 2016, Immiscible iron- and silica-rich melts and magnetite geochemistry at the El Laco volcano (northern Chile): Evidence for a magmatic origin for the magnetite deposits: Ore Geology Reviews, v. 79, p. 346-366.

Von Gruenewaldt, G., Klemm, D., Henckel, J., and Dehm, R., 1985, Exsolution features in titanomagnetites from massive magnetite layers and their host rocks of the Upper Zone, Eastern Bushveld Complex: Economic Geology, v. 80, p. 1049-1061.

Watson, E.B., and Liang, Y., 1995, A simple model for sector zoning in slowly grown crystals: Implications for growth rate and lattice diffusion, with emphasis on accessory minerals in crustal rocks: American Mineralogist, v. 80, p. 1179-1187.

Wawryk, C., 2017, An investigation into iron isotope systematics in felsic magmas and their associated magmatic-hydrothermal ore deposits: Unpub. PhD. dissertation thesis, University of Adelaide, Australia.

Wen, G., Li, J.-W., Hofstra, A.H., Koenig, A.E., Lowers, H.A., and Adams, D., 2017, Hydrothermal reequilibration of igneous magnetite in altered granitic plutons and its implications for magnetite classification schemes: Insights from the Handan-Xingtai iron district, North China Craton: Geochimica et Cosmochimica Acta, v. 213, p. 255-270.

Whitney, J.A., Hemley, J.J., and Simon, F.O., 1985, The concentration of iron in chloride solutions equilibrated with synthetic granitic compositions; the sulfur-free system: Economic Geology, v. 80, p. 444-460.

Williams, P.J., Barton, M.D., Johnson, D.A., Fontbote, L., De Haller, A., Mark, G., Oliver, N.H.S., and Marschik, R., 2005, Iron oxide copper-gold deposits: geology, space-time distribution and possible modes of origin, *in* Hedenquist, J. W., Thompson, J. F. H., Goldfarb, R. J., and Richards, J. P., eds., Economic Geology 100th Aniversary Volume: Littelton, Colorado, USA, Society of Economic Geologists, p. 371-405.

Xavier, R.P., Monteiro, L.V.S., Moreto, C.P.N., Pestilho, A.L.S., De Melo, G.H.C., Da Silva, M.A.D., Aires, B., Ribeiro, C., and E Silva, F.H.F., 2012, The iron oxide copper-gold systems of the Carajás mineral province, Brazil: Economic Geology Special Publication 16, p. 433-454.

Xia, F., Brugger, J., Chen, G., Ngothai, Y., O'Neill, B., Putnis, A., and Pring, A., 2009,

Mechanism and kinetics of pseudomorphic mineral replacement reactions: a case study of the replacement of pentlandite by violarite: Geochimica et Cosmochimica Acta, v. 73, p. 1945-1969.

Xu, H., Shen, Z., and Konishi, H., 2014, Si-magnetite nano-precipitates in silician magnetite from banded iron formation: Z-contrast imaging and ab initio study: American Mineralogist, v. 99, p. 2196-2202.

Yin, S., Ma, C., and Robinson, P.T., 2017, Textures and high field strength elements in hydrothermal magnetite from a skarn system: Implications for coupled dissolution-reprecipitation reactions: American Mineralogist, v. 102, p. 1045-1056.

Zhao, W.W., and Zhou, M.-F., 2015, In-situ LA–ICP-MS trace elemental analyses of magnetite: The Mesozoic Tengtie skarn Fe deposit in the Nanling Range, South China: Ore Geology Reviews, v. 65, p. 872-883.

Zhao, X.-F., and Zhou, M.-F., 2011, Fe-Cu deposits in the Kangdian region, SW China: a Proterozoic IOCG (iron-oxide–copper–gold) metallogenic province: Mineralium Deposita, v. 46, p. 731-747.

Zhao, X.-F., Zhou, M.-F., Gao, J.-F., Li, X.-C., and Li, J.-W., 2015, In situ Sr isotope analysis of apatite by LA-MC-ICPMS: constraints on the evolution of ore fluids of the Yinachang Fe-Cu-REE deposit, Southwest China: Mineralium Deposita, v. 50, p. 871-884.

Figure captions

Fig. 1. Photomicrographs of ores from selected IOCG and IOA deposits showing mineral association and magnetite textures. All images are acquired by back-scattered electron (BSE) imaging except those in (E) and (H) by reflected light. (A) Sample 080 from the Sossego IOCG deposit composed of euhedral to subhedral magnetite and apatite and minor chalcopyrite cut by a quartz and calcite assemblage. (B) Sample 080 from the Sossego IOCG deposit consisting of magnetite, apatite, chlorite, and talc. Magnetite has exsolution lamellae of ilmenite and contains calcite, chalcopyrite, and chlorite microinclusions. Granular ilmenite is also associated with magnetite. The inset at upper right is enlargement of the area marked by yellow rectangle. (C) Sample 084 from the Sossego IOCG deposit composed of magnetite and apatite cut by quartz and chalcopyrite veins. (D) Sample F392 from the Igarapé Bahia IOCG deposit has a mineral association of magnetite, chlorite, siderite, and chalcopyrite. (E) Sample Alemao from the Alemao IOCG deposit composed of magnetite and apatite cut by calcite and quartz. Magnetite shows core-rim texture with inclusion-rich core and inclusion-free rim. (F) Ore from the Alemao IOCG deposit consisting of subhedral magnetite and accessory apatite replaced by quartz, chlorite, and minor chalcopyrite. (G) Sample SAL2 from the Salobo IOCG deposit composed of magnetite and chalcopyrite, and minor quartz and grunerite. (H) Sample 11CC051 from the Salobo IOCG deposit comprising subhedral magnetite replaced by chlorite, chalcopyrite and quartz. Magnetite shows foam-like texture. (I) Sample 367A from the Candelaria IOCG deposit composed of magnetite, K-feldspar, actinolite, and minor albite and biotite. (J) Sample PC98102 from the Candelaria IOCG deposit consisting of

magnetite and chalcopyrite, and minor chlorite, biotite, and monazite. (K) Sample PC1492 from the Candelaria IOCG deposit composed of magnetite, chalcopyrite, K-feldspar, and actinolite. Magnetite is commonly cut by chlorite veins. (L) Sample El Romeral from the El Romeral IOA deposit consisting of magnetite and actinolite, and minor biotite and chlorite. Abbreviations: Act = actinolite, Ab = Albite, Ap = apatite, Bt = biotite, Cal = calcite, Ccp = chalcopyrite, Chl = chlorite, Gru = grunerite, Kfs = K-feldspar, Mag = magnetite, Mnz = monazite, Qz = quartz, Sd = siderite, Tlc = talc.

Fig. 2. BSE images showing textures of magnetite from the Sossego, Igarapé Bahia and Alemao IOCG deposits. (A) Three generations of magnetite identified in sample 080 from the Sossego IOCG deposit. The first generation of magnetite (Mag-1) with exsolution lamellae of ilmenite was overgrown by smooth, light gray magnetite (Mag-2). Mag-2 was further replaced by dark gray magnetite (Mag-3) along the fracture. Amphibole inclusions are mainly distributed along the boundary between Mag-1 and Mag-2, whereas rutile inclusions are mainly within Mag-1. (B) Two generations of magnetite in sample 080 from the Sossego IOCG deposit displaying different textures. The first magnetite with exsolution lamellae of ilmenite in the core (Mag-1) was replaced by dark gray, inclusion-rich magnetite (Mag-3). Inclusions in Mag-3 are mainly quartz and rutile. (C) Two generations of magnetite in sample 084 from the Sossego IOCG deposit. The first generation of magnetite contains ilmenite and hercynite inclusions, and shows oscillatory zoning composed of dark gray

(Mag-1D) and light gray (Mag-1L) zones. The second generation of magnetite (Mag-2) crosscut both Mag-1D and Mag-1L and contains silicate inclusions. (D) Magnetite grain in sample 084 from the Sossego IOCG deposit characterized by oscillatory zoning composed of dark gray (Mag-1D) and light gray (Mag-1L) zones. Ilmenite, hercynite, and actinolite are mainly inclusions in magnetite. (E) Magnetite in sample F392 from the Igarapé Bahia IOCG deposit composed of inclusion-rich (Mag-1) and inclusion-poor (Mag-2) domains. The inclusions in Mag-1 are mainly siderite and chalcopyrite. (F) Magnetite in Alemao IOCG deposit consisting of inclusion-rich core (Mag-1) and inclusion-poor rim (Mag-2). Both Mag-1 and Mag-2 are crosscut by later calcite veins. The inclusions in Mag-1 are mainly quartz, chlorite, and chalcopyrite. Abbreviations: Act = actinolite, Amp = amphibole, Cal = calcite, Ccp = chalcopyrite, Chl = chlorite, Hc = hercynite, Ilm = ilmenite, Mag = magnetite, Qz = quartz, Rt = rutile, Sd = siderite.

Fig. 3. BSE images showing textures of magnetite from the Candelaria and Salobo IOCG and El Romeral IOA deposits. (A) Sample 367A from the Candelaria IOCG deposit showing two generations of magnetite. The first generation of magnetite (Mag-1) is dark gray and inclusion-rich, which was replaced by smooth, inclusion-poor magnetite (Mag-2). Some grains also show triple junction textures (yellow lines).Titanite and quartz are main inclusions in Mag-1. (B) Sample PC1492 from the Candelaria IOCG deposit comprising dark gray, inclusion-rich (Mag-1) and light gray, inclusion-poor magnetite (Mag-2). Inclusions in Mag-1 are mainly biotite

and albite. (C) Magnetite in sample SAL2 from the Salobo IOCG deposit composed of dark gray (Mag-1) and light gray (Mag-2) domains. (D) Three generations of magnetite in El Romeral IOA deposit showing different textures. The primary magnetite (Mag-1) is inclusion-rich and replaced by secondary magnetite (Mag-2). Mag-2 is further replaced by dark gray magnetite (Mag-3) along the grain boundary or fractures. (E-F) Magnetite in sample 11CC051 from the Salobo IOCG deposit and sample PC98102 from the Candelaria IOCG deposit composed of inclusion-rich (Mag-1) and inclusion-poor (Mag-2) domains. Chlorite and quartz are the main inclusions in Mag-1. Yellow lines indicate triple junction textures. Abbreviations: Act = actinolite, Ab = albite, Bt = biotite, Ccp = chalcopyrite, Chl = chlorite, Mag = magnetite, Qz = quartz, Rt = rutile.

Fig. 4. BSE images and chemical X-ray maps of sample 080 from the Sossego IOCG deposit. Magnetite generations in A and B correspond to A and B in Fig. 2, respectively. The scales of X-ray maps are the same as that of corresponded BSE images. (A) Three generations of magnetite showing different Ti, Al, Si, Ca, Mg, and Mn contents. Mag-1 has the highest Ti contents due to the exsolution of ilmenite, whereas Mag-2 and Mag-3 have the lower but relatively homogeneous Ti contents. Silicon, Ca, and Mg contents increase from Mag-2, Mag-1, to Mag-3. Mag-1 and Mag-3 have similar Al and Mn contents that are higher than Mag-2. Iron contents between different generations of magnetite are indistinguishable in terms of available resolution. (B) Two generations of magnetite showing different Ti, Al, Si, Ca, and Mn

contents. Mag-1 contains exsolution lamellae of ilmenite indicated by anomalously high Ti contents. Mag-3 has higher Si and Ca but lower Al, Ti and Mn contents than Mag-1. Iron and Mg contents in two generations of magnetite are indistinguishable.

Fig. 5. BSE images and chemical X-ray maps of sample 084 from the Sossego IOCG deposit. Magnetite generations in A and B correspond to C and D in Fig. 2, respectively. (A) The first generation of magnetite composed of Mag-1D and Mag-1L and containing ilmenite and hercynite inclusions indicated by characteristic distribution of Ti and Al contents. The first generation of magnetite shows Al, Si, Ca, and Mg chemical zoning. Both Mag-1D and Mag-1L were replaced by Mag-2. Mag-1 has higher Ti, Al, Si, Ca, and Mg contents than Mag-2. (B) Magnetite with oscillatory zoning composed of dark gray (Mag-1D) and light gray (Mag-1L) domains. The oscillatory zoning shows consistent changes in Al, Si, Ca, and Mg contents. No systematic variations in Fe and Ti contents between Mag-1D and Mag-1L are observed, but the whole magnetite grain shows heterogeneous Ti contents.

Fig. 6. BSE images and X-ray maps of selected elements in magnetite. Magnetite generations in (A) and (B) correspond to (E) and (F) in Fig. 2, respectively, whereas magnetite generations in (C) and (D) correspond to (A) and (B) in Fig. 3, respectively. (A) Dark gray, inclusion-rich magnetite (Mag-1) in sample F392 from the Igarapé Bahia IOCG deposit containing more Si and Mg and less Fe than light, inclusion-poor magnetite (Mag-2). No obvious variation in Ti contents is observed between two

generations of magnetite. (B) Dark gray, inclusion-rich cores (Mag-1) in magnetite from the Alemao IOCG deposit having higher Si and Mg, but lower Fe contents than light gray, inclusion-poor rims (Mag-2). Titanium, Al, and Ca contents are indistinguishable between two generations of magnetite under available resolution. (C-D) Dark gray, inclusion-rich magnetite domains (Mag-1) in samples 367A and PC1492 from the Candelaria IOCG deposit having higher Si and Mg contents but lower Fe contents than light gray, smooth magnetite domains (Mag-2). Titanium contents are similar in both generations of magnetite.

Fig. 7. BSE images and chemical X-ray maps of samples, El Romeral (A), 11CC051 (B), and PC98102 (C), from the El Romeral IOA, Salobo and Candelaria IOCG deposits, respectively. Magnetite generations in (A), (B), and (C) correspond to (D), (E), and (F) in Fig. 3, respectively. (A) Three generations of magnetite showing different chemical compositions. Mag-1 and Mag-3 have lower Fe but higher Mg contents than Mag-2. Silicon, Ca and Al contents increase from Mag-2, Mag-1, to Mag-3. Moreover, Si, Ca and Al contents are not homogeneous in Mag-3. No obvious differences in Ti contents between different generations of magnetite. The inclusions in Mag-1 are mainly silicate minerals characterized by higher Si, Mg, Al and/or Ca contents. (B-C) Inclusion-rich magnetite domains (Mag-1) showing higher Si, Mg and Mn contents than inclusion-poor magnetite domains (Mag-2).

Fig. 8. Multi-element box and whisker plots for EPMA minor and trace element data

showing the compositional differences between different magnetite generations. Boxes outline the 25th to 75th percentiles and whiskers extend to the minimum and maximum values. Short line within the box represents the median value, whereas circle filled by white on the whisker represents the average value. Trace element contents below the limit of detection were excluded in the box and whisker plots.

Fig. 9. Multi-element box and whisker plots for EPMA minor and trace element data showing the compositional differences between different magnetite generations. The meaning of box is the same as in Fig. 8.

Fig. 10. Box and whisker plot for Fe contents in different generations of magnetite. The meaning of box is the same as in Fig. 8.

Fig. 11. Schematic illustrations showing different chemical or physical processes responsible for the formation of multiple generations of magnetite in IOCG and IOA deposits. These processes include oxy-exsolution (OE), coupled dissolution reprecipitation (CDR), and recrystallization (RC). Fragmentation (FR) and overgrowth (OG) is also involved in some magnetite. (A) High-Ti magnetite (Mag-1) from the Sossego IOCG deposit (sample 084) shows oscillatory zoning with dark gray, Si-rich (Mag-1D) and light gray, Si-poor zones (Mag-1L). High-Ti magnetite was further replaced by secondary magnetite (Mag-2) via type 1 CDR process. Ilmenite and hercynite formed as inclusions in Mag-1 because of Ti-Al-rich fluids. Both first

and second magnetite has experienced fragmentation. (B) High-Ti magnetite (Mag-1) from the Sossego IOCG deposit (sample 080) experienced widespread oxy-exsolution of ilmenite. Mag-2 may have formed by overgrowth, whereas Mag-3 formed by type 2 CDR process. (C) Low-Ti magnetite in the Alemao IOCG deposit with abundant inclusions of siderite, quartz, chlorite, or chalcopyrite experienced type 1 CDR process to form inclusion-rich core (Mag-1) and inclusion-poor rim (Mag-2). Some of the cores evolved to inclusion-absent with the progressive type 1 CDR process. Fragmentation is also common due to volume change during mineral growth. (D) Low-Ti magnetite with silicate inclusions in samples F392 and PC1492 from the Igarapé Bahia and Candelaria IOCG deposits, respectively experienced one or multiple type 1 CDR processes, forming the secondary magnetite as stockworks. (E) Si-rich magnetite from the Salobo IOCG deposit (SAL2) suffered from type 1 CDR process, resulting in the formation of Si-poor magnetite. Quartz formed along the boundary between Mag-1 and Mag-2. (F) Low-Ti magnetite from the Candelaria IOCG (samples 367A and PC98102), Salobo IOCG (sample 11CC051), and El Romeral IOA (sample El Romeral) deposits experienced types 1 and 2 CDR processes and recrystallization, forming two or three generations of magnetite. See text for detail. Abbreviations: Act = actinolite, Amp = amphibole, Ccp = chalcopyrite, Chl = chlorite, Hc = hercynite, Ilm = ilmenite, Mag = magnetite, Qz = quartz, Rt = rutile, Sd = siderite, Ttn = titanite.

Fig. 12. Binary plots showing compositional variations during different reequilibrium

processes. (A) Plot of V versus Ti showing decreased Ti and increased V contents in magnetite during oxy-exsolution. Chemical composition of magnetite before exsolution is the average LA-ICP-MS data of Huang et al. (2019). (B) Plot of Fe versus Si+K+Ca+Al+Mn+Mg showing decreased contents of minor and trace elements and increased Fe contents during type 1 CDR process. (C) Plot of Fe versus Si+K+Ca+Al+Mn+Mg showing increased contents of minor and trace elements during type 2 CDR process. (D) Plot of Fe versus Si+K+Ca+Al+Mn+Mg showing indistinguishable variations in trace element and Fe contents during recrystallization.

Fig. 13. Plot of EPMA data of IOCG and IOA deposits in the Ti+V vs. Ca+Al+Mn diagram. (A) Compositional variations between different generations of magnetite from the Sossego IOCG deposit. The decreased Ti+V and Ca+Al+Mn contents of Mag-1 in samples 080 and 084 (Mag-1D and Mag-1L) to Mag-2 are due to decreasing temperature and changing melt/fluid composition. During type 2 CDR process, Ca+Al+Mn contents in magnetite increase but Ti+V contents are relatively stable. (B) Compositional variations between different generations of magnetite from the El Romeral IOA deposit, induced by various fluid compositions or type 2 CDR process. (C) Compositional variations in magnetite during type 1 CDR process. During this process, Ca+Al+Mn contents decrease to various degrees but Ti+V contents keep constant. (D) No obvious compositional differences between primary magnetite (Mag-1) and recrystallized magnetite (Mag-2). EPMA data of sample Chadormalu in (D) are individual analyses from Chadormalu IOA deposit (Heidarian et al., 2016),

whereas data of CIB are average values from Chilean iron belt (Nyström and Henríquez, 1994). The fields for different deposit types are based on Dupuis and Beaudoin (2011). If the content of one of the elements Ti, V, Ca, Al, and Mn is lower than the detection limit, data are plotted as hollow symbol. The temperatures near the top abscissa are from Nadoll et al. (2014) where temperatures of magnetite crystallization in a variety of ore deposits were compiled. Deposit type abbreviations: Skarn = Fe-Cu skarn deposits, IOCG = iron oxide–copper–gold deposits, Porphyry = porphyry Cu deposits; Kiruna = Kiruna-type magnetite-apatite deposits.

Fig. 14. Plot of EPMA data of IOCG and IOA deposits in the magnetite discrimination diagrams used to distinguish magnetite from magnetite-apatite ores, titaniferous iron ores, and BIF (Loberg and Horndahl, 1983). (A) Plot of V vs. Ni. (B) Plot of V/Ti vs. Ni/Ti. (C) Plot of V vs. Ti. (D) V/Fe (ppm/wt%) vs. Ti/Fe (ppm/wt%). Data below detection limits are removed from these plots. Pink circle with dotted line represents the field of Chadormalu IOA deposit (Bafq district of Central Iran) (Heidarian et al., 2016), whereas orange circle with dotted line represents the field of Kiruna and Rektorn (Norrbotten region of Sweden), and El Laco (Chile) IOA deposits (Broughm et al., 2017). Gray area represents the composition range of magnetite from El Romeral IOA deposit.

Tables

Table 1. Summary of Information on Samples from the Studied IOCG and IOA

Deposits

Table A1. Chemical Composition of Magnetite (in wt%) from the IOCG and IOA Deposits

Figures

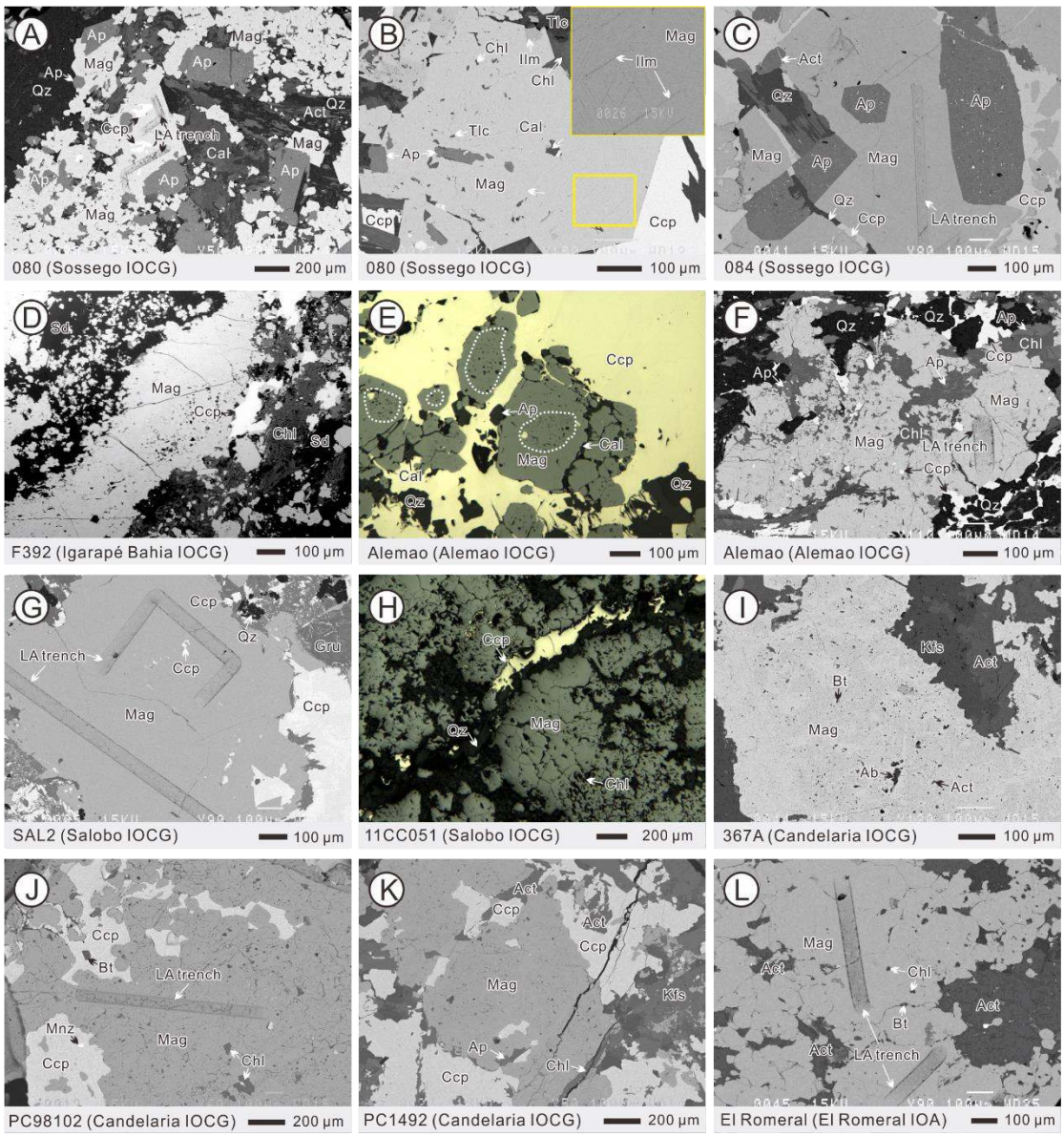

Fig. 1

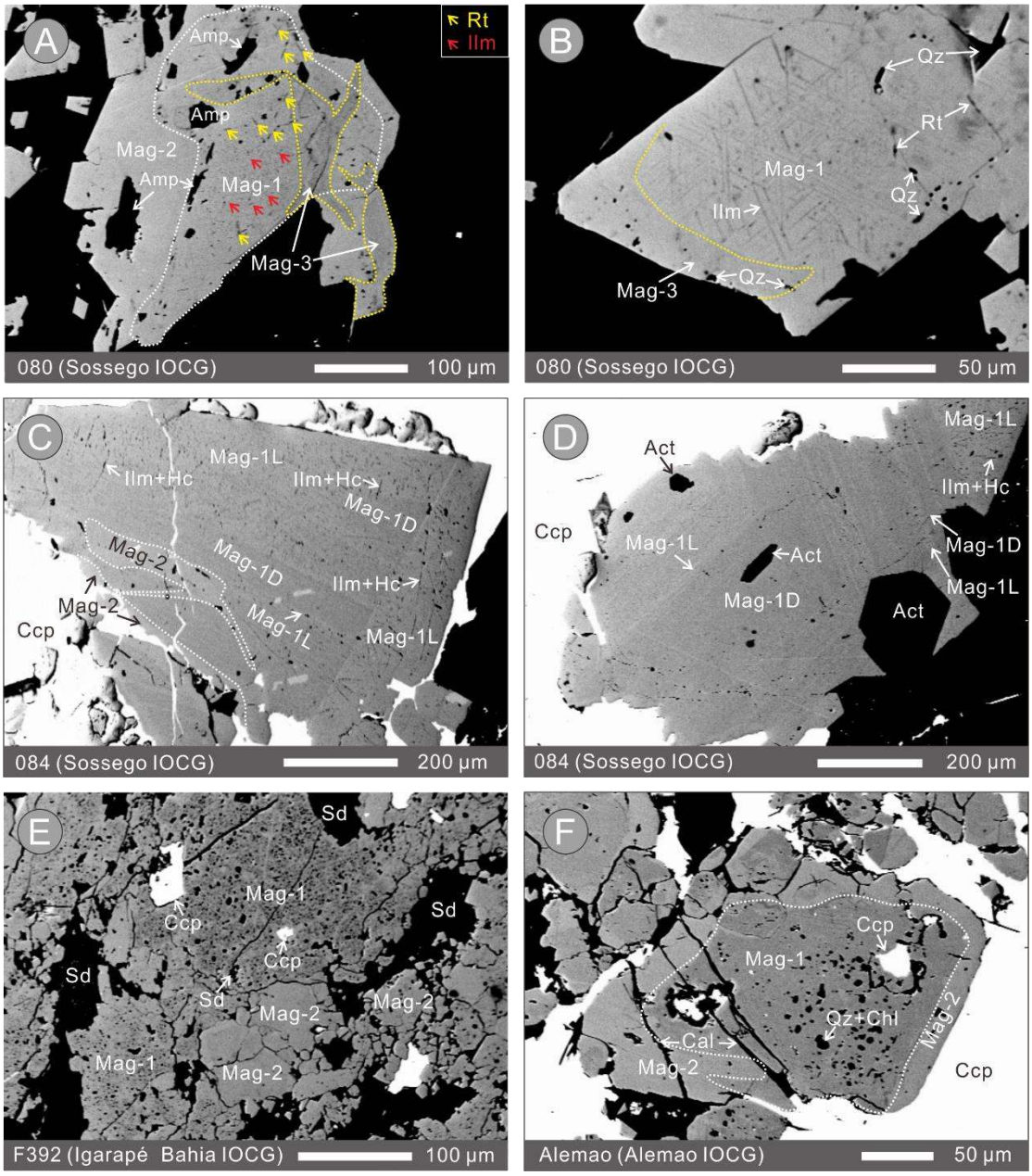
A
Rt
Ilm
Amp
Amp
Mag-2
Amp
Mag-1
Mag-3
080 (Sossego IOCG)
100 µm
B
Qz
Rt
Mag-1
Ilm
Qz
Mag-3
Qz
080 (Sossego IOCG)
50 µm
C
Mag-1L
Ilm+Hc
Ilm+Hc
Mag-1D
Mag-2
Mag-1D
Ilm+Hc
Mag-2
Mag-1L
Ccp
Mag-1L
084 (Sossego IOCG)
200 µm
D
Act
Mag-1L
Ilm+Hc
Ccp
Mag-1L
Act
Mag-1D
Mag-1D
Act
Mag-1L
084 (Sossego IOCG)
200 µm
E
Sd
Mag-1
Ccp
Sd
Ccp
Sd
Sd
Mag-2
Mag-2
Mag-1
Mag-2
F392 (Igarapé Bahia IOCG)
100 µm
F
Ccp
Mag-1
Qz+Chl
Mag-2
Cal
Mag-2
Ccp
Alemao (Alemao IOCG)
50 µm

Fig. 2

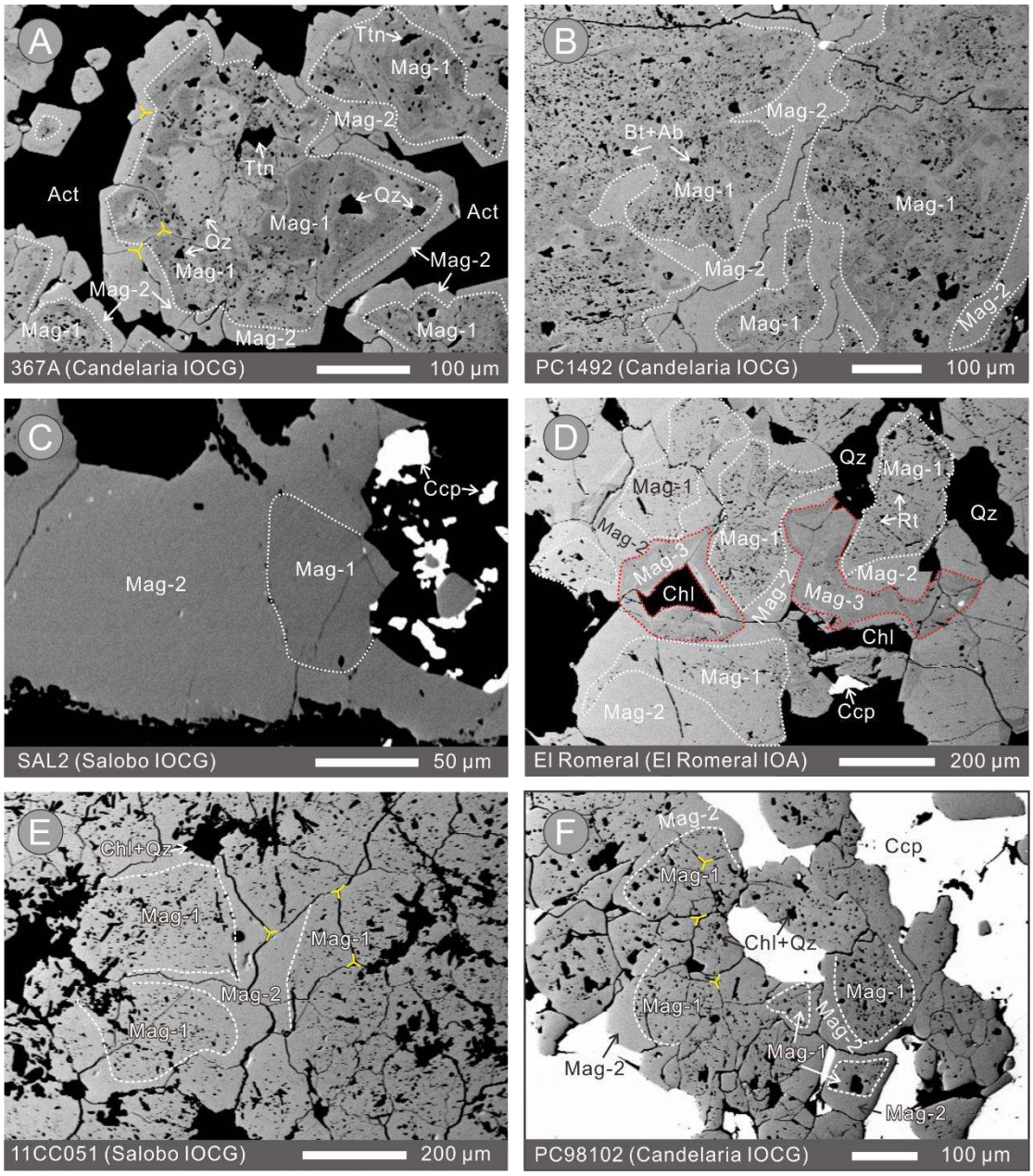
A
Ttn
Mag-1
Mag-2
Ttn
Act
Qz
Act
Mag-1
Qz
Mag-1
Mag-2
Mag-2
Mag-1
Mag-2
Mag-1
367A (Candelaria IOCG)
100 µm
B
Mag-2
Bt+Ab
Mag-1
Mag-1
Mag-2
Mag-1
Mag-2
PC1492 (Candelaria IOCG)
100 µm
C
Ccp
Mag-2
Mag-1
SAL2 (Salobo IOCG)
50 µm
D
Qz
Mag-1
Mag-1
Rt
Qz
Mag-2
Mag-3
Mag-1
Chl
Mag-2
Mag-2
Mag-3
Chl
Mag-1
Mag-2
Ccp
El Romeral (El Romeral IOA)
200 µm
E
Chl+Qz
Mag-1
Mag-1
Mag-2
Mag-1
11CC051 (Salobo IOCG)
200 µm
F
Mag-2
Ccp
Mag-1
Chl+Qz
Mag-1
Mag-1
Mag-2
Mag-1
Mag-2
PC98102 (Candelaria IOCG)
100 µm

Fig. 3

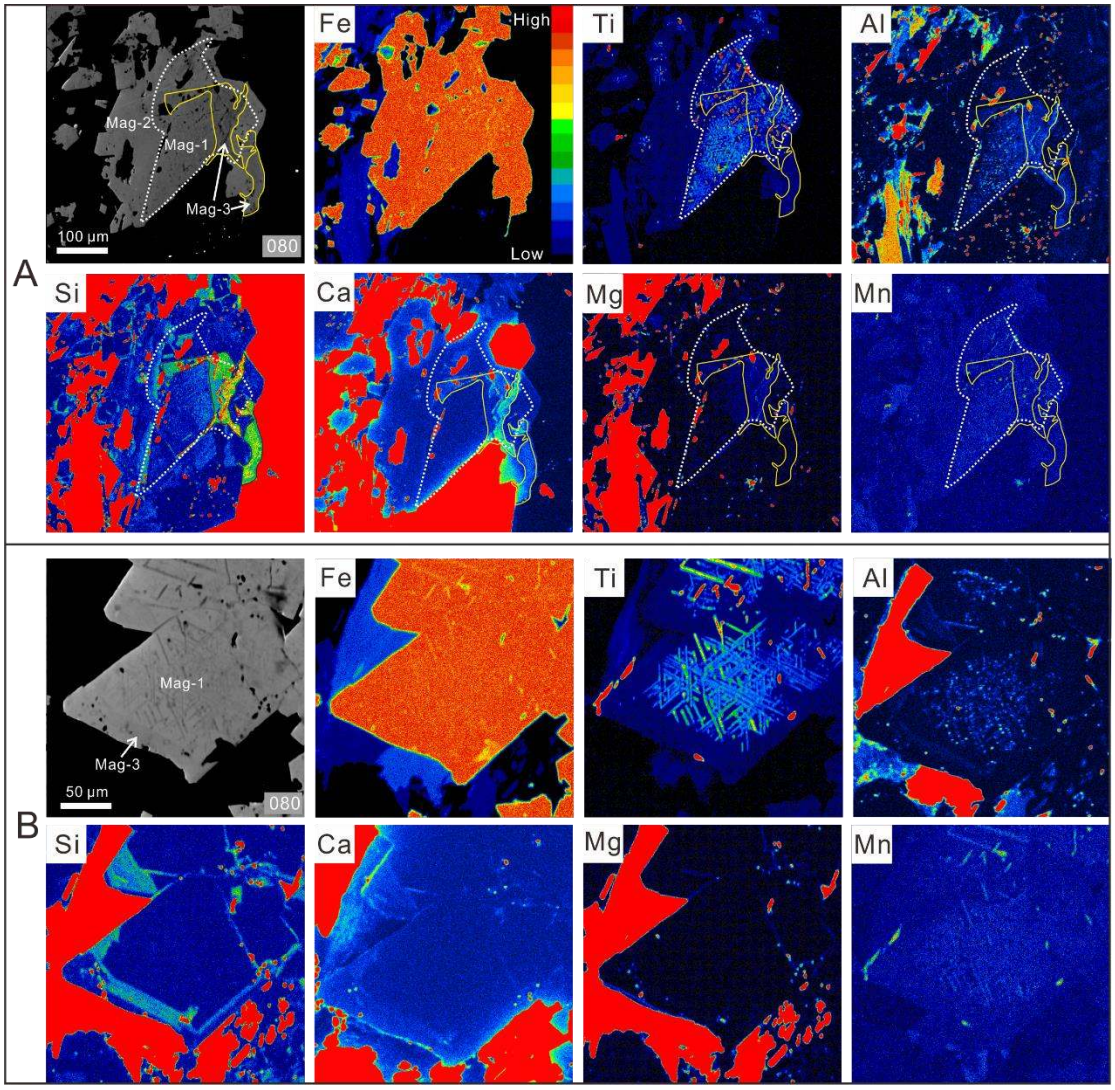
A
Mag-2
Mag-1
Mag-3
100 μm
080
Fe
High
Low
Ti
Al
Si
Ca
Mg
Mn
B
Mag-1
Mag-3
50 μm
080
Fe
Ti
Al
Si
Ca
Mg
Mn

Fig. 4

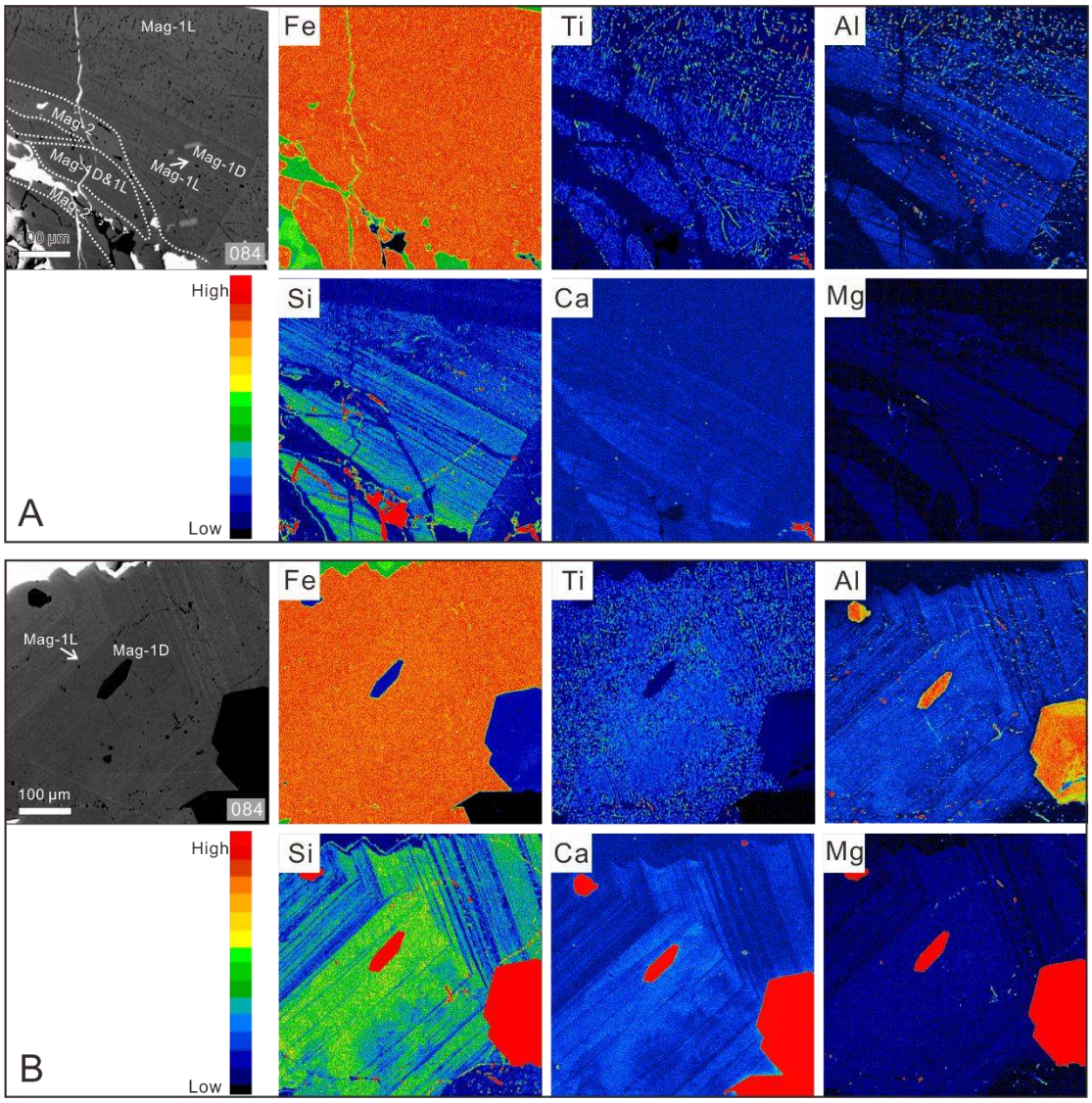
Mag-1L
Mag-2
Mag-1D&1L
Mag-1D
Mag-1L
Mag-2
100 µm
084
Fe
Ti
Al
High
Low
Si
Ca
Mg
A
Mag-1L
Mag-1D
100 µm
084
Fe
Ti
Al
High
Low
Si
Ca
Mg
B

Fig. 5

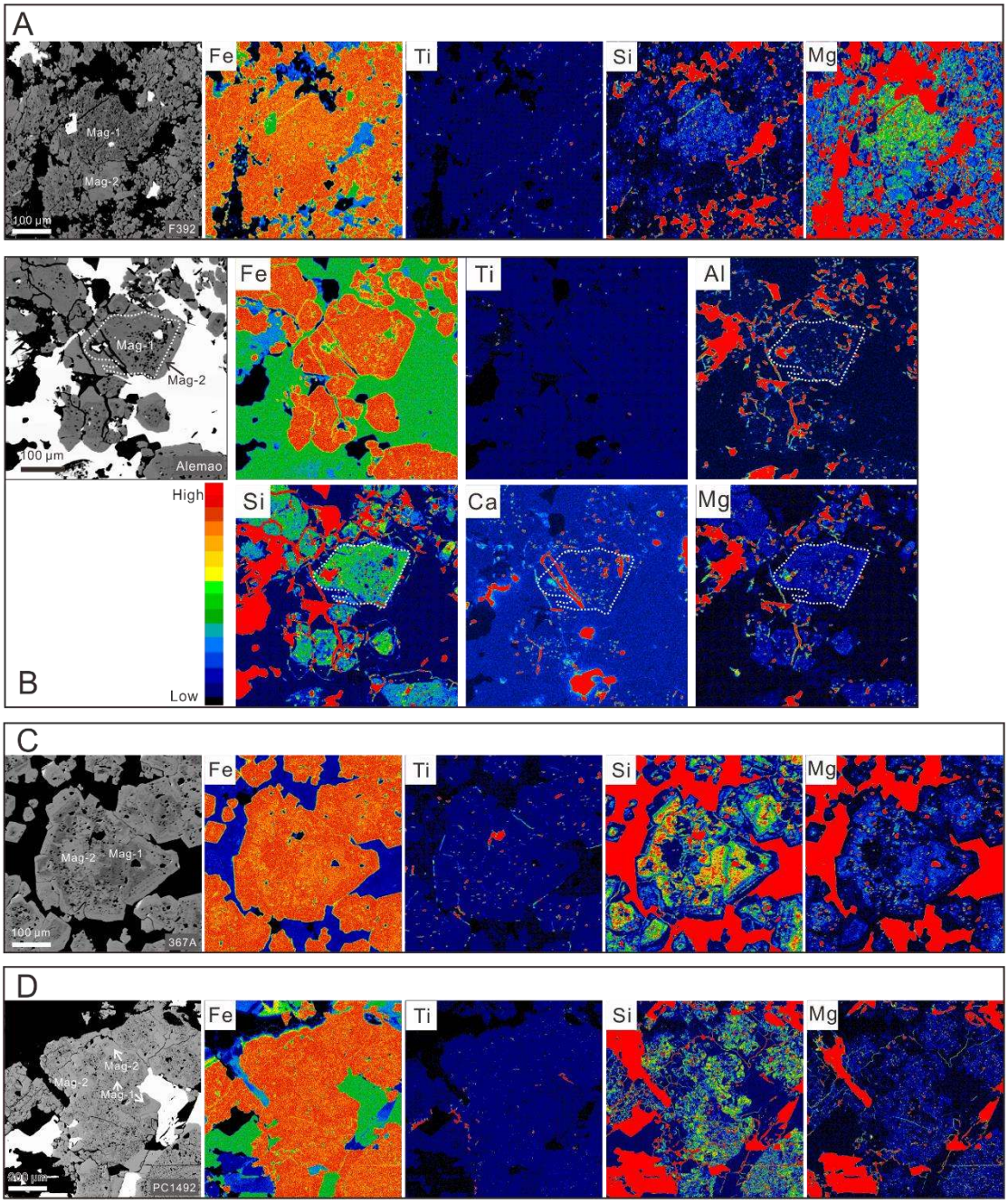
A
Fe
Ti
Si
Mg
Mag-1
Mag-2
100 µm
F392
Fe
Ti
Al
Mag-1
Mag-2
100 µm
Alemao
High
Low
Si
Ca
Mg
B
C
Fe
Ti
Si
Mg
Mag-2
Mag-1
100 µm
367A
D
Fe
Ti
Si
Mg
Mag-2
Mag-2
Mag-1
100 µm
PC1492

Fig. 6

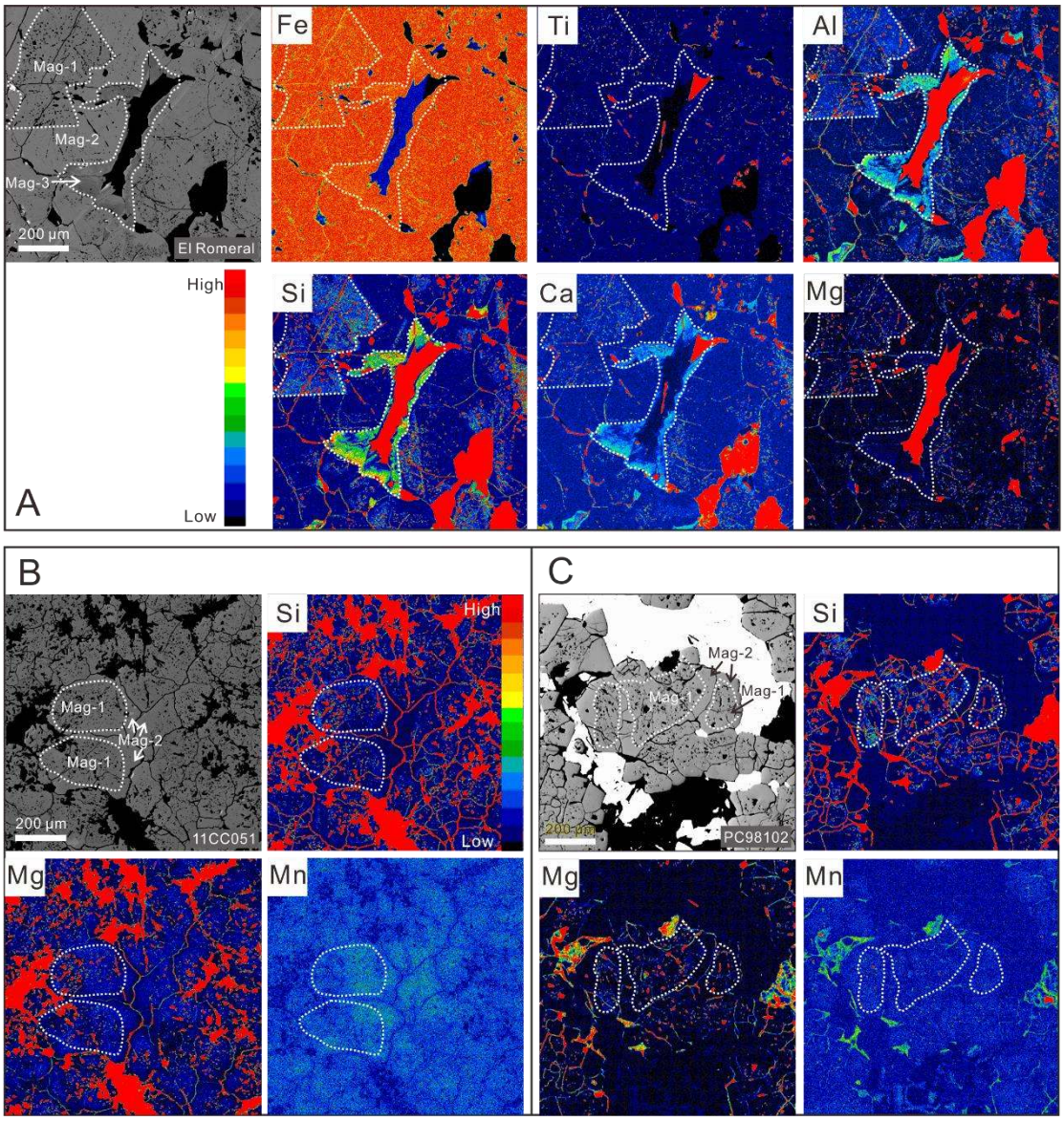
Mag-1
Mag-2
Mag-3
200 µm
El Romeral
Fe
Ti
Al
High
Low
A
Si
Ca
Mg
B
Si
High
Low
Mag-1
Mag-2
Mag-1
200 µm
11CC051
Mg
Mn
C
Mag-2
Mag-1
Mag-1
200 µm
PC98102
Si
Mg
Mn

Fig. 7

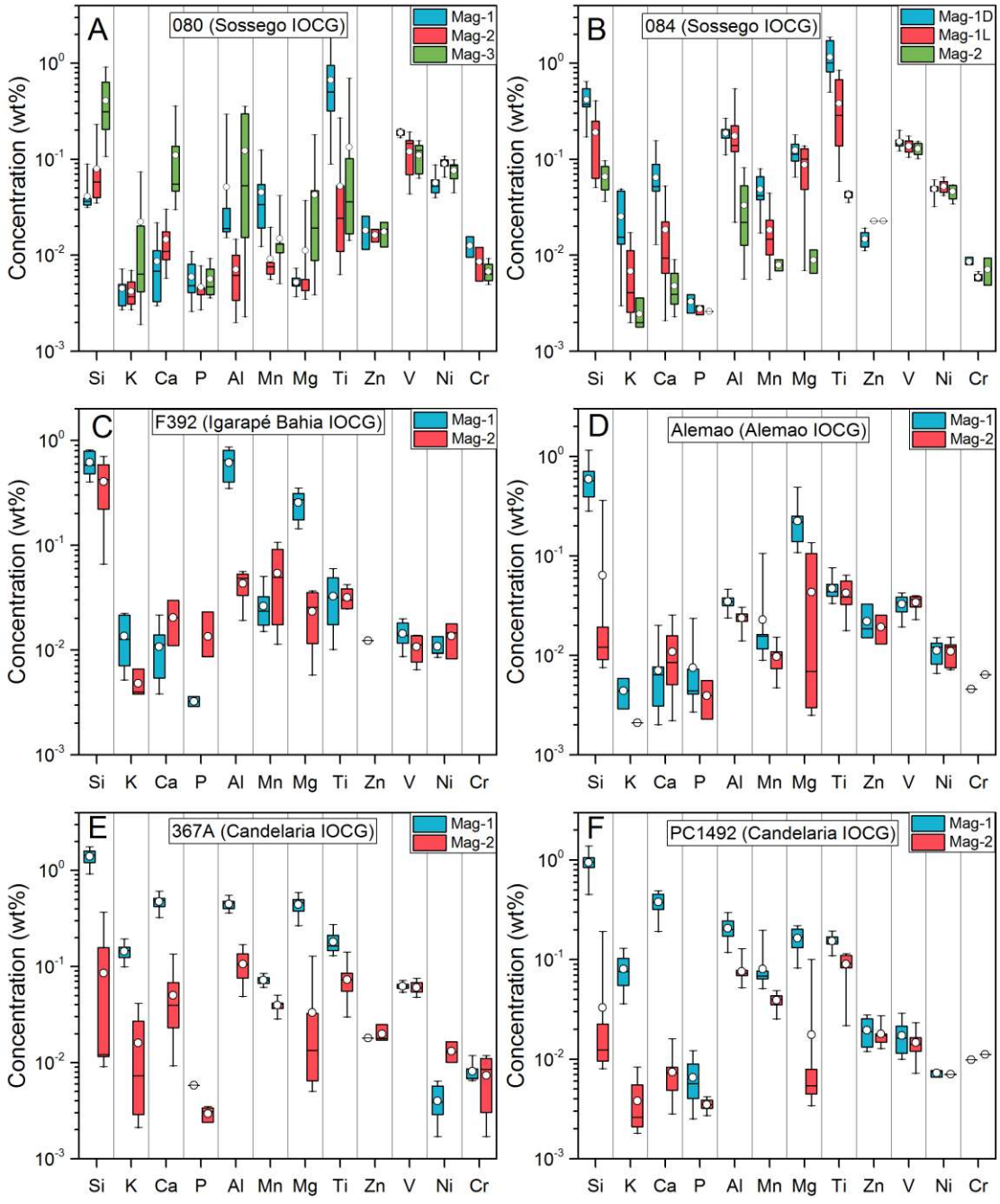
A
080 (Sossego IOCG)
Mag-1
Mag-2
Mag-3
B
084 (Sossego IOCG)
Mag-1D
Mag-1L
Mag-2
C
F392 (Igarapé Bahia IOCG)
Mag-1
Mag-2
D
Alemao (Alemao IOCG)
Mag-1
Mag-2
E
367A (Candelaria IOCG)
Mag-1
Mag-2
F
PC1492 (Candelaria IOCG)
Mag-1
Mag-2
Concentration (wt%)
Si K Ca P Al Mn Mg Ti Zn V Ni Cr

Fig. 8

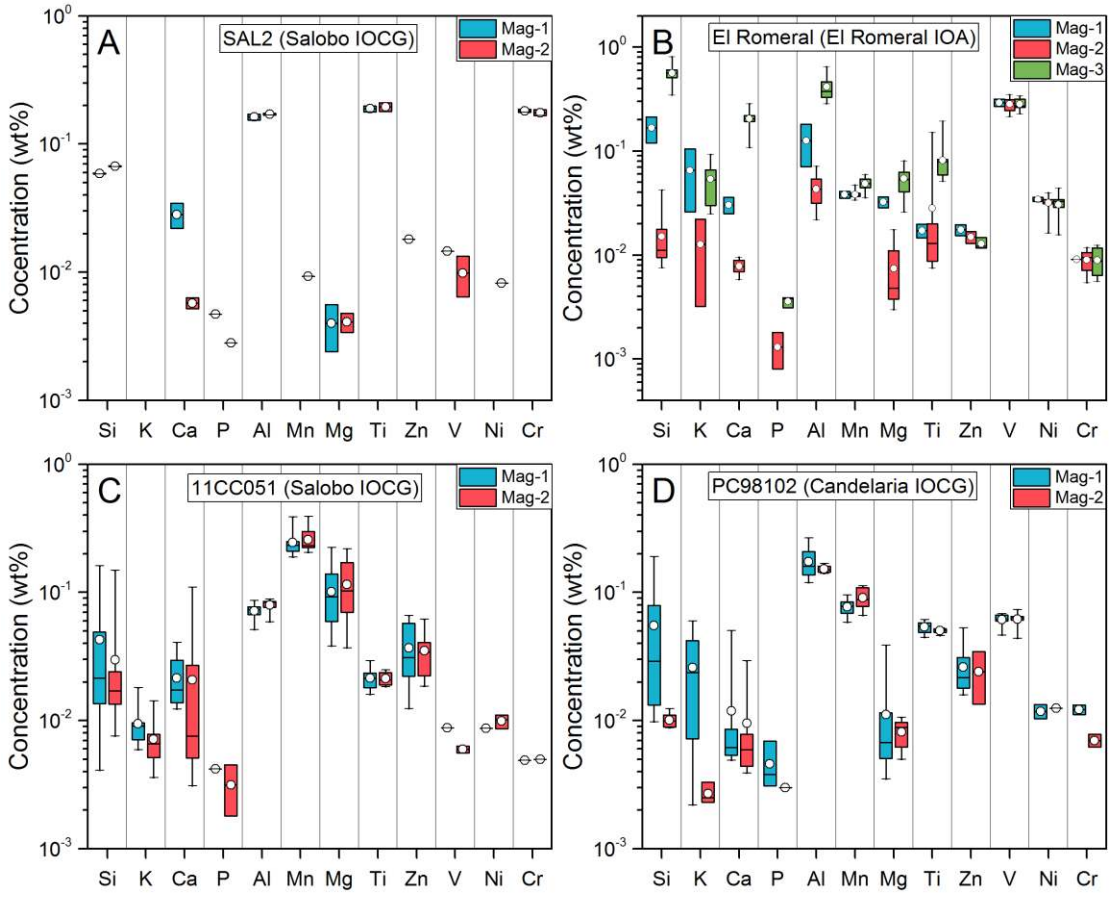
A
SAL2 (Salobo IOCG)
Mag-1
Mag-2
Cocentration (wt%)
B
El Romeral (El Romeral IOA)
Mag-1
Mag-2
Mag-3
Concentration (wt%)
C
11CC051 (Salobo IOCG)
Mag-1
Mag-2
Concentration (wt%)
D
PC98102 (Candelaria IOCG)
Mag-1
Mag-2
Concentration (wt%)
Si K Ca P Al Mn Mg Ti Zn V Ni Cr

Fig. 9

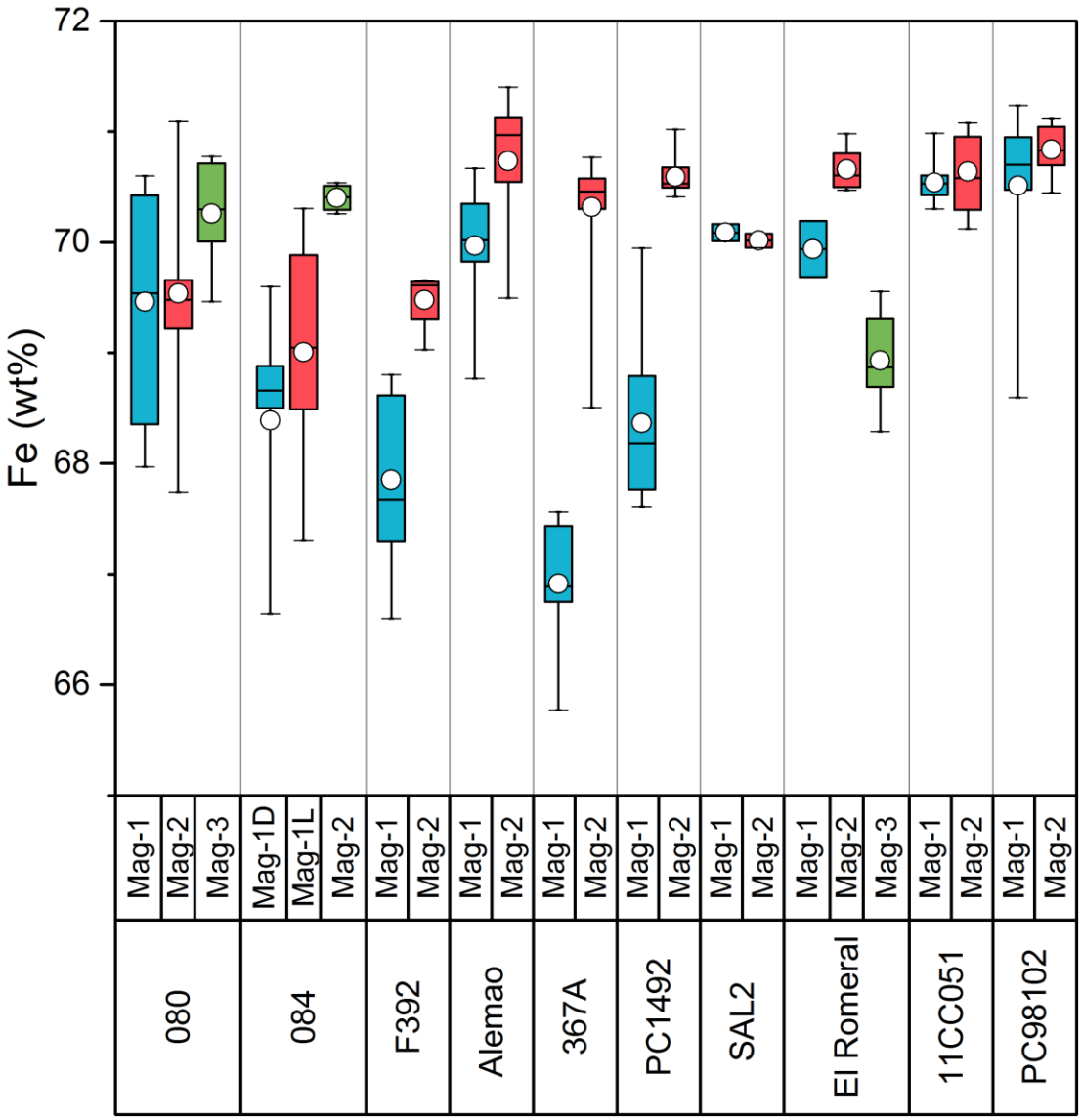
Fe (wt%)
72
70
68
66
Mag-1
Mag-2
Mag-3
Mag-1D
Mag-1L
Mag-2
Mag-1
Mag-2
Mag-1
Mag-2
Mag-1
Mag-2
Mag-1
Mag-2
Mag-1
Mag-2
Mag-1
Mag-2
Mag-3
Mag-1
Mag-2
Mag-1
Mag-2
080
084
F392
Alemao
367A
PC1492
SAL2
El Romeral
11CC051
PC98102

Fig. 10

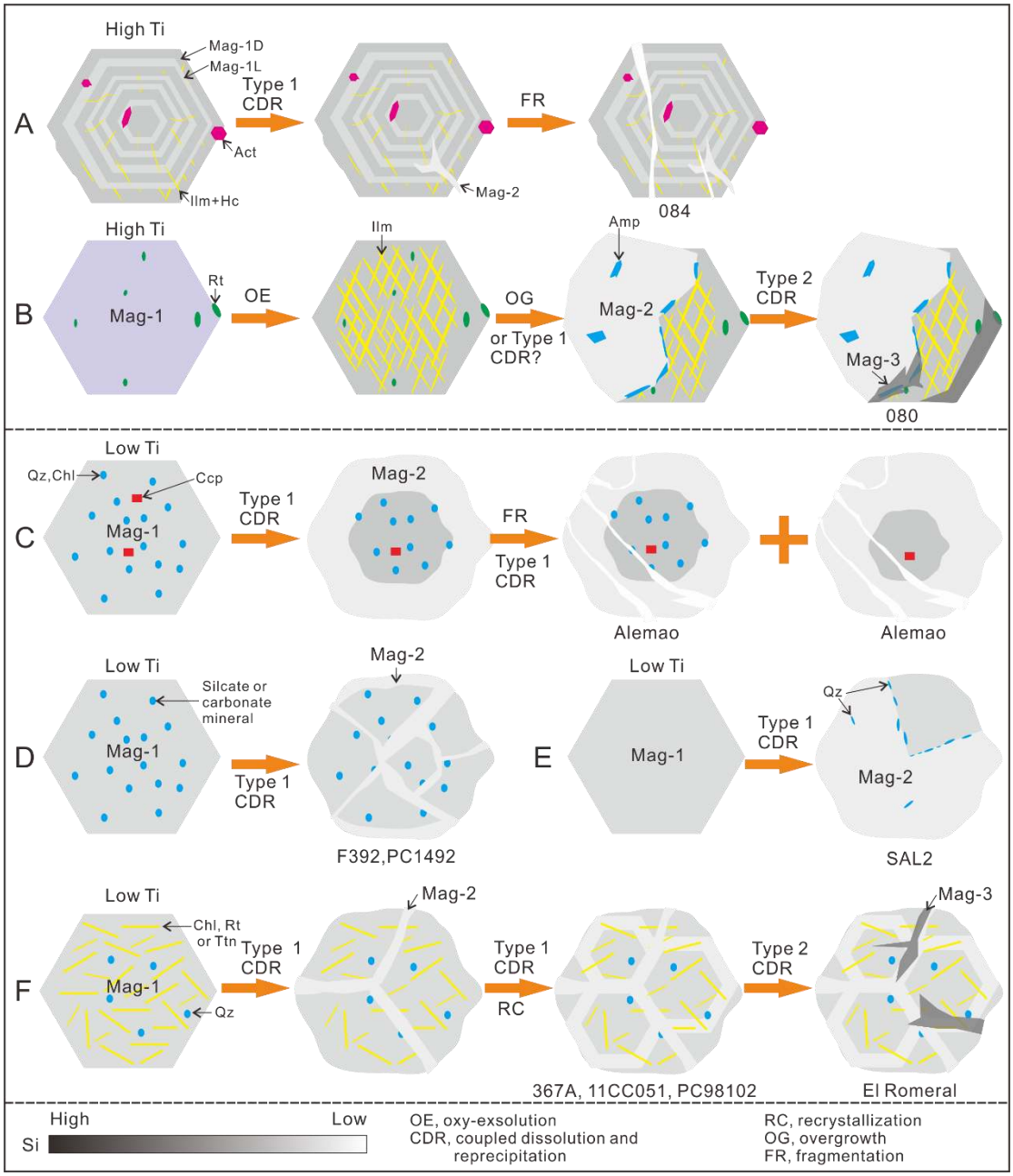
A
High Ti
Mag-1D
Mag-1L
Type 1
CDR
Act
Ilm+Hc
FR
Mag-2
084
B
High Ti
Mag-1
Rt
OE
Ilm
OG
or Type 1
CDR?
Amp
Mag-2
Type 2
CDR
Mag-3
080
C
Low Ti
Qz,Chl
Ccp
Mag-1
Type 1
CDR
Mag-2
FR
Type 1
CDR
Alemao
Alemao
D
Low Ti
Silcate or
carbonate
mineral
Mag-1
Type 1
CDR
Mag-2
F392,PC1492
E
Low Ti
Mag-1
Type 1
CDR
Qz
Mag-2
SAL2
F
Low Ti
Chl, Rt
or Ttn
Mag-1
Qz
Type 1
CDR
Mag-2
Type 1
CDR
RC
Type 2
CDR
Mag-3
367A, 11CC051, PC98102
El Romeral
High
Si
Low
OE, oxy-exsolution
CDR, coupled dissolution and
reprecipitation
RC, recrystallization
OG, overgrowth
FR, fragmentation

Fig. 11

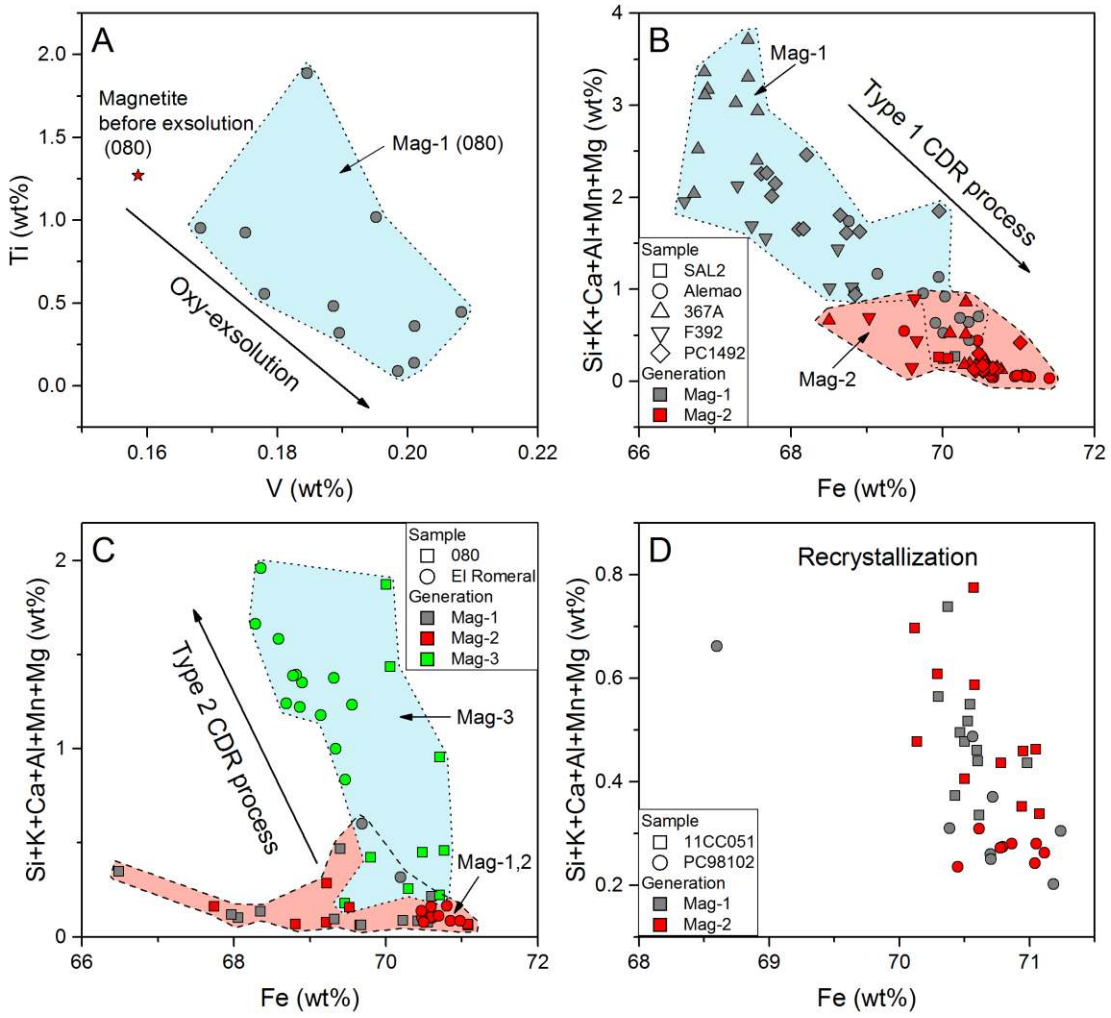
A
Magnetite
before exsolution
(080)
Mag-1 (080)
Oxy-exsolution
Ti (wt%)
V (wt%)
B
Mag-1
Type 1 CDR process
Mag-2
Sample
SAL2
Alemao
367A
F392
PC1492
Generation
Mag-1
Mag-2
Si+K+Ca+Al+Mn+Mg (wt%)
Fe (wt%)
C
Sample
080
El Romeral
Generation
Mag-1
Mag-2
Mag-3
Type 2 CDR process
Mag-3
Mag-1,2
Si+K+Ca+Al+Mn+Mg (wt%)
Fe (wt%)
D
Recrystallization
Sample
11CC051
PC98102
Generation
Mag-1
Mag-2
Si+K+Ca+Al+Mn+Mg (wt%)
Fe (wt%)

Fig. 12

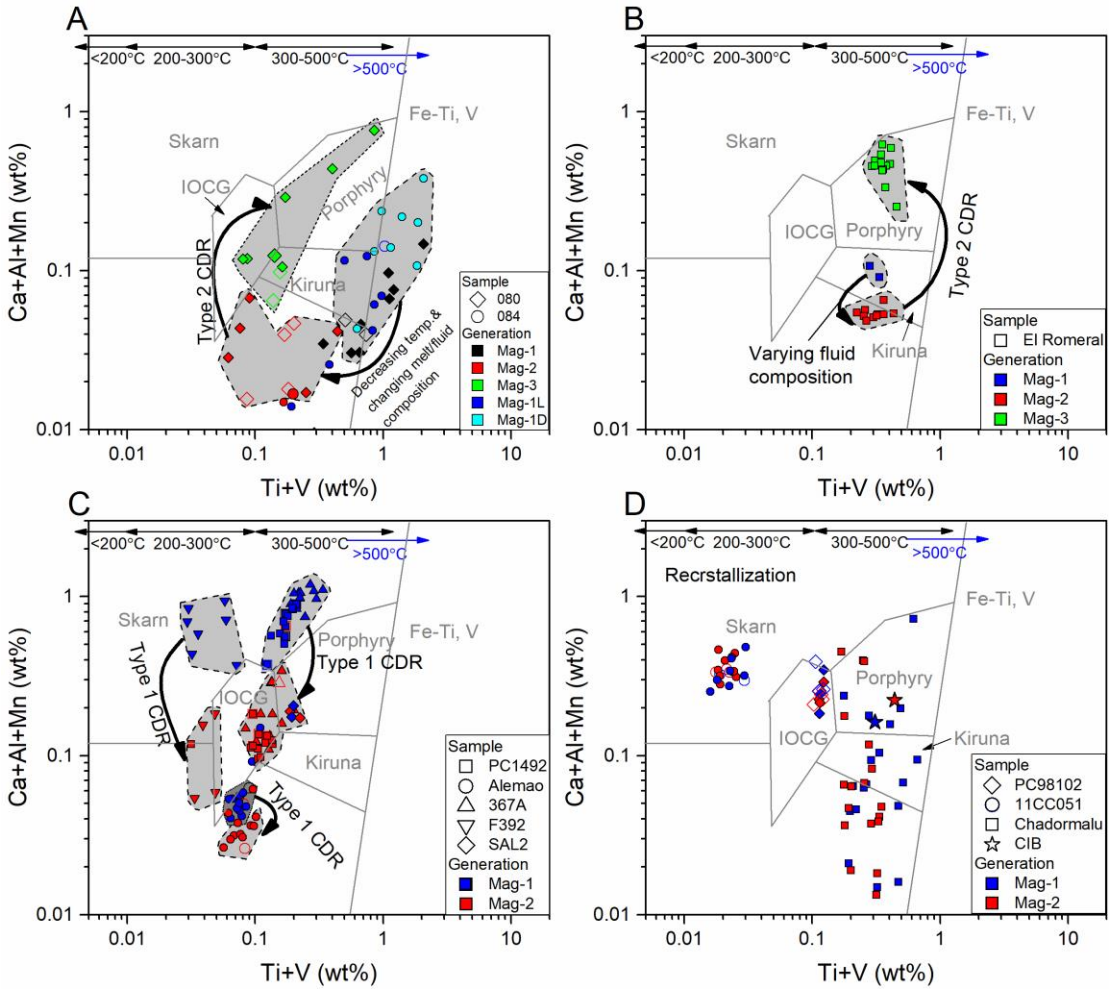
A
<200°C 200-300°C 300-500°C >500°C
Fe-Ti, V
Skarn
IOCG
Porphyry
Kiruna
Type 2 CDR
Decreasing temp & changing melt/fluid composition
Sample
080
084
Generation
Mag-1
Mag-2
Mag-3
Mag-1L
Mag-1D
Ca+Al+Mn (wt%)
Ti+V (wt%)
B
<200°C 200-300°C 300-500°C >500°C
Fe-Ti, V
Skarn
IOCG
Porphyry
Type 2 CDR
Varying fluid composition
Kiruna
Sample
El Romeral
Generation
Mag-1
Mag-2
Mag-3
Ca+Al+Mn (wt%)
Ti+V (wt%)
C
<200°C 200-300°C 300-500°C >500°C
Skarn
Type 1 CDR
Porphyry
Fe-Ti, V
Type 1 CDR
IOCG
Kiruna
Type 1 CDR
Sample
PC1492
Alemao
367A
F392
SAL2
Generation
Mag-1
Mag-2
Ca+Al+Mn (wt%)
Ti+V (wt%)
D
<200°C 200-300°C 300-500°C >500°C
Recrstallization
Fe-Ti, V
Skarn
Porphyry
IOCG
Kiruna
Sample
PC98102
11CC051
Chadormalu
CIB
Generation
Mag-1
Mag-2
Ca+Al+Mn (wt%)
Ti+V (wt%)

Fig. 13

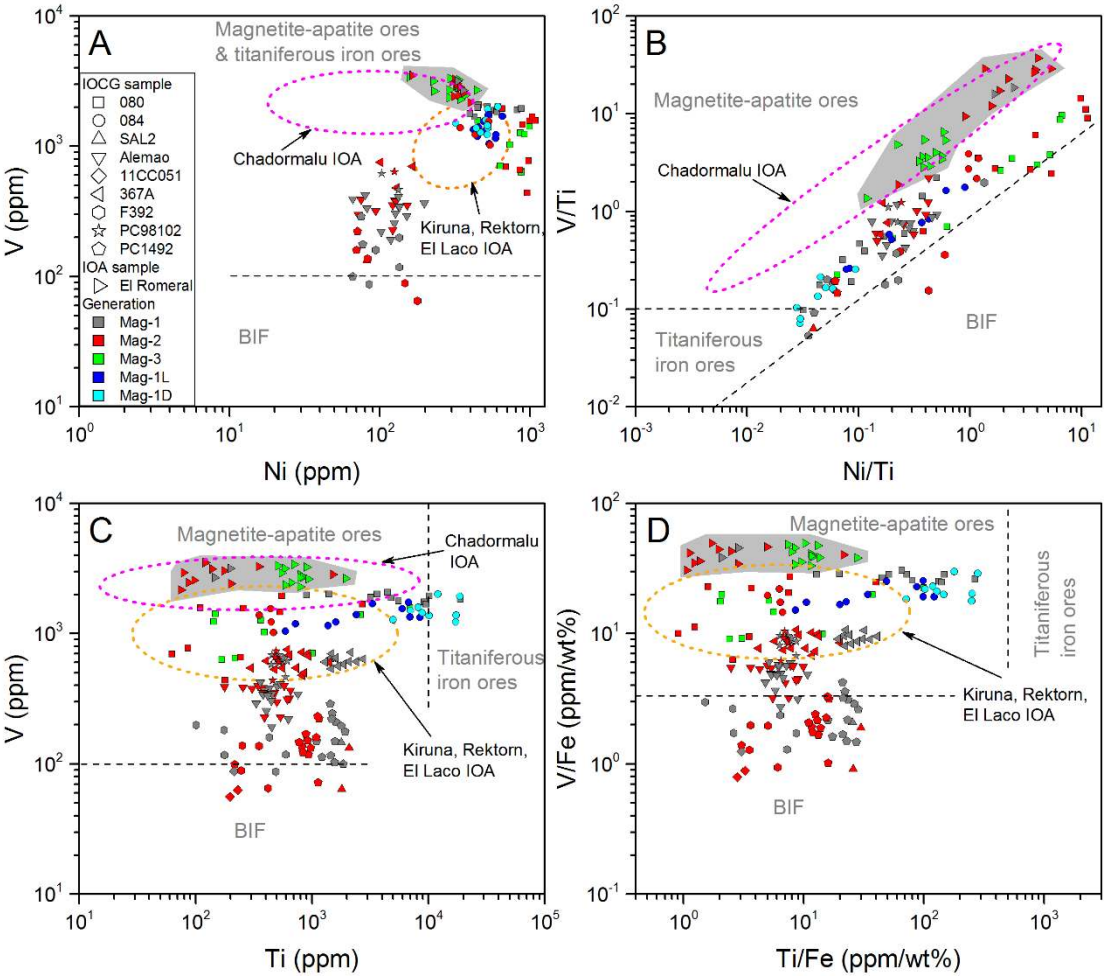
A
Magnetite-apatite ores
& titaniferous iron ores
IOCG sample
080
084
SAL2
Alemao
11CC051
367A
F392
PC98102
PC1492
IOA sample
El Romeral
Generation
Mag-1
Mag-2
Mag-3
Mag-1L
Mag-1D
Chadormalu IOA
Kiruna, Rektorn,
El Laco IOA
BIF
V (ppm)
Ni (ppm)
B
Magnetite-apatite ores
Chadormalu IOA
Titaniferous
iron ores
BIF
V/Ti
Ni/Ti
C
Magnetite-apatite ores
Chadormalu
IOA
Titaniferous
iron ores
Kiruna, Rektorn,
El Laco IOA
BIF
V (ppm)
Ti (ppm)
D
Magnetite-apatite ores
Titaniferous
iron ores
Kiruna, Rektorn,
El Laco IOA
BIF
V/Fe (ppm/wt%)
Ti/Fe (ppm/wt%)

Fig. 14

Table 1. Summary of Information on Samples from the Studied IOCG and IOA Deposits

Deposit name	Deposit type	Sample no.	Host rock	Age (Ga)	Metallic mineral	Gangue mineral	Mineral inclusion in magnetite	Magnetite generations	Magnetite textures	References
Igarapé Bahia, Brazil	IOCG	F392	Archean volcano-sedimentary rocks	2.57	Mag, Ccp, Py	Sd, Cal	Sd	Mag-1, 2	CDR	Tallarico et al. (2005)
Alemao, Brazil	IOCG	Alemao	Archean volcano-sedimentary rocks	2.57	Mag, Hem, Ccp, Py	Ap, Bt, Chl, Cal, Qz	Qz, Cal, Chl	Mag-1, 2	CDR	Ronzê et al. (2000)
Sossego, Brazil	IOCG	080	Archean volcano-sedimentary rocks	1.90-1.88	Mag, Ilm, Ccp, Po, Py	Ap, Amp, Act, Qz, Cal, Chl	Amp, Ap, Act, Chl	Mag-1, 2, 3	OE, CDR	Monteiro et al. (2008a, b); Moreto et al. (2015)
		084			Mag, Ilm, Ccp, Po, Py	Ap, Act, Qz, Cal, Chl	Ap, Act	Mag-1D, 1L, 2	OZ, CDR	
Salobo, Brazil	IOCG	SAL2	Archean volcano-sedimentary rocks	2.58	Mag, Ccp, Cct, Bn, Py	Bt, Fa, Fl, Gru, Qz, Tur, Chl	Ccp, Bt, Chl	Mag-1, 2	CDR	Requia and Fontboté (2000)
		11CC051			Mag, Ccp, Py	Bt, Grt, Chl, Qz	Chl, Qz	Mag-1, 2	RC	
Candelaria, Chile	IOCG	367A	Early Cretaceous volcanic rocks	0.12	Mag, Ccp, Py	Bt, Amp, Ap, Act, Ttn, Chl, Ep	Chl, Ttn, Bt, Act	Mag-1, 2	CDR, RC	Marschik and Fontboté (2001);
		PC98102			Mag,	Bt, Chl,	Chl, Qz	Mag-1, 2	RC	Mathur et al.

		PC1492			Ccp, Py Mag, Ccp, Py	Cal, Qz Kfs, Bt, Ab, Ap, Ttn	Bt, Ab, Kfs	Mag-1, 2	CDR	(2002)
El Romeral, Chile	IOA	El Romeral	Cretaceous volcanic rocks	0.13-0.10	Mag	Act, Ab, Chl	Ab, Chl	Mag-1, 2, 3	CDR, RC	Bookstorm, 1977; Alva-Valdivia et al. (2003)

Notes: Samples 080 and 084 are from Sossego–Curral orebodies of the Sossego deposit. OE = oxy-exsolution; OZ = oscillatory zoning; CDR = coupled dissolution and reprecipitation; RC = recrystallization

Mineral abbreviations: Ab = albite, Act = actinolite, Amp = amphibole, Ap = apatite, Bn = bornite, Bt = biotite, Cal = calcite, Ccp = chalcopyrite, Cct = chalcocite, Chl = chlorite, Fa = fayalite, Fl = fluorite, Grt = garnet, Gru = grunerite, Hem = hematite, Ilm = ilmenite, Kfs = K-feldspar, Mag = magnetite, Po = pyrrhotite, Py = pyrite, Qz = quartz, Sd = siderite, Ttn = titanite

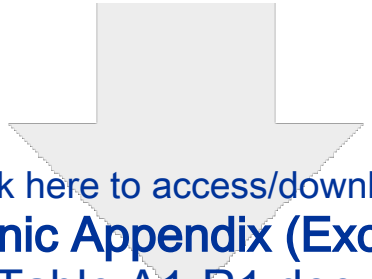

Click here to access/download

Electronic Appendix (Excel etc.)

Table A1-R1.docx